

ICE ACCRETION PREDICTION ON WIND TURBINE BLADES AND  
AERODYNAMIC SHAPE OPTIMIZATION FOR MINIMIZING POWER  
PRODUCTION LOSSES

A THESIS SUBMITTED TO  
THE GRADUATE SCHOOL OF NATURAL AND APPLIED SCIENCES  
OF  
MIDDLE EAST TECHNICAL UNIVERSITY

BY

ÖZCAN YIRTICI

IN PARTIAL FULFILLMENT OF THE REQUIREMENTS  
FOR  
THE DEGREE OF DOCTOR OF PHILOSOPHY  
IN  
AEROSPACE ENGINEERING

SEPTEMBER 2018



Approval of the thesis:

**ICE ACCRETION PREDICTION ON WIND TURBINE BLADES AND  
AERODYNAMIC SHAPE OPTIMIZATION FOR MINIMIZING POWER  
PRODUCTION LOSSES**

submitted by **ÖZCAN YIRTICI** in partial fulfillment of the requirements for the degree of **Doctor of Philosophy in Aerospace Engineering Department, Middle East Technical University** by,

Prof. Dr. Halil Kalıpçılar  
Dean, Graduate School of **Natural and Applied Sciences** \_\_\_\_\_

Prof. Dr. Ozan Tekinalp  
Head of Department, **Aerospace Engineering** \_\_\_\_\_

Prof. Dr. İsmail Hakkı Tuncer  
Supervisor, **Aerospace Engineering Department, METU** \_\_\_\_\_

Prof. Dr. Serkan Özgen  
Co-supervisor, **Aerospace Engineering Department, METU** \_\_\_\_\_

**Examining Committee Members:**

Prof. Dr. Oğuz Uzol  
Aerospace Engineering Department, METU \_\_\_\_\_

Prof. Dr. İsmail Hakkı Tuncer  
Aerospace Engineering Department, METU \_\_\_\_\_

Prof. Dr. Zafer Dursunkaya  
Mechanical Engineering Department, METU \_\_\_\_\_

Assist. Prof. Dr. Mustafa Kaya  
Aeronautical Engineering Department, YBU \_\_\_\_\_

Assist. Prof. Dr. Durmuş Sinan Körpe  
Aeronautical Engineering Department, UTAA \_\_\_\_\_

Date: 07.09.2018

**I hereby declare that all information in this document has been obtained and presented in accordance with academic rules and ethical conduct. I also declare that, as required by these rules and conduct, I have fully cited and referenced all material and results that are not original to this work.**

Name, Last Name: Özcan Yırtıcı

Signature :

## ABSTRACT

### **ICE ACCRETION PREDICTION ON WIND TURBINE BLADES AND AERODYNAMIC SHAPE OPTIMIZATION FOR MINIMIZING POWER PRODUCTION LOSSES**

Yırtıcı, Özcan

Ph.D., Department of Aerospace Engineering

Supervisor : Prof. Dr. İsmail Hakkı Tuncer

Co-Supervisor : Prof. Dr. Serkan Özgen

September 2018, 80 pages

The global wind energy resources are plentiful in cold climate regions and mountainous areas, which cause ice formation on wind turbine blades. Prediction of ice accretion on wind turbine blades makes it possible to estimate the power losses due to icing. Ice accretion on wind turbine blades is responsible for significant increases in aerodynamic drag and decreases in aerodynamic lift, and may even cause premature flow separation. All these events create power losses and the amount of power loss depends on the severity of icing and the turbine blade profile shape. The main objective of this study is to develop a cost-effective and accurate numerical methodology to predict ice accretion on horizontal axis wind turbines and ice-induced power losses under various icing conditions. In addition, a gradient based aerodynamic shape optimization is performed to minimize the power production loss due to ice accretion.

The Extended Messinger Model is implemented for the prediction of ice accretion on blade profiles, and the Blade Element Momentum Methodology is implemented

for the prediction of power production of clean and iced wind turbines. The role of critical parameters such as wind speed, temperature and liquid water content on ice accretion is studied in detail. The predicted ice shapes on various airfoil profiles are validated against available experimental and numerical data in literature. It is shown that the tool developed may effectively be used in the prediction of power production losses of wind turbines at representative atmospheric icing conditions. In the optimization study, the blade profile is modified by using bump functions around the leading edge of the blade profile, and it is shown that the optimized blade profile reduces the power production loss due to icing.

**Keywords:** Wind Energy, Atmospheric Icing, Ice Accretion, Computational Fluid Dynamics, Gradient Method, Aerodynamic Optimization.

## ÖZ

### **RÜZGAR TÜRBİN PALLERİNDE BUZ BİRİKİM TAHMİNİ VE GÜÇ ÜRETİM KAYIPLARINI DÜŞÜRMEK İÇİN AERODİNAMİK ŞEKİL ENİYİLEMESİ**

Yırtıcı, Özcan

Doktora, Havacılık ve Uzay Mühendisliği Bölümü

Tez Yöneticisi : Prof. Dr. İsmail Hakkı Tuncer

Ortak Tez Yöneticisi : Prof. Dr. Serkan Özgen

Eylül 2018 , 80 sayfa

Dünya çapında rüzgar enerjisi kaynakları soğuk iklim bölgelerinde ve dağlık arazilerde bolca bulunmasına rağmen rüzgar türbin pallerinde buzlanmaya neden olur. Rüzgar türbin palasında buz şekillerini tahmin edebilmek buzlanma kaynaklı güç üretim kayıplarını hesaplamayı olanaklı hale getirmiştir. Rüzgar türbin pallerinde buz birikimi kaydadeğer bir şekilde aerodinamik sürüklenme kuvvetinde bir artışa ve aerodinamik kaldırma kuvvetinde bir azalışa neden olur, ve hatta erken akış ayrışmasına sebep olabilir. Tüm bu olaylar güç kayıplarını doğurur ve bu kayıpların miktarı buzlanmanın şiddetine ve türbin pala profiline bağlıdır. Bu çalışmanın amacı, yatay eksenli rüzgar türbinlerinde farklı buzlanma koşulları altında buz birikim tahmini ve buna bağlı güç kayıplarını efektif ve doğru bir şekilde sayısal bir yöntem geliştirerek hesaplamaktır. Ayrıca, gradyen tabanlı aerodinamik şekil eniyileştirme yapılarak buz birikimi kaynaklı güç kaybını minimize etmektir.

Pala profillerinde buz birikim tahmini yapmak için Genişletilmiş Messinger Modeli ve temiz ve buzlanmış rüzgar türbinlerinde güç üretim tahmini için Pal Elemanı-

Momentum (Blade Element Momentum - BEM) Teorisi uygulanmıştır. Rüzgar hızı, sıcaklık ve sıvı su içeriği gibi kritik parametrelerin buzlanma boyut ve şekilleri üzerindeki rolü detaylı bir şekilde analiz edilmiştir. Değişik kanat profilleri üzerinde tahmin edilen buz şekilleri literatürde bulunan deneysel ve sayısal veriler karşısında doğrulandı. Bu geliştirilen aracın benzer atmosferik buzlanma koşullarında rüzgar türbin güç üretim kayıplarını etkin bir biçimde tahmin etmekte kullanılabileceği gösterilmiştir. Eniyileştirme sürecinde pala profili bump fonksiyonları kullanılarak hücum kenarı civarında modifiye edildi ve eniyileştirme sabit rüzgar hızında gerçekleştirildi. Eniyileştirilmiş pala profilinin buzlanma nedenli güç üretim kaybını azalttığı ve bu azalışın eniyileştirme koşulları altında daha etkin sonuç verdiği görülmüştür.

Anahtar Kelimeler: Rüzgar Enerjisi, Atmosferik Buzlanma, Buz Birikimi, Hesaplamalı Akışkanlar Dinamiği, Gradyan Yöntemi, Aerodinamik Eniyileme.

To my dearest parents and sister, Madiye, Hikmet and Özlem

## ACKNOWLEDGMENTS

First of all, I would like to give special thanks to my advisor, Prof. Dr. İsmail H. Tuncer for his guidance, support and helpful discussions that we have made throughout the study. Through his guidance, I have gained invaluable experience and insight related to not only in CFD but also in wind energy. I could not have had a better advisor.

I would also like to thank to my co-supervisor Prof. Dr. Serkan Özgen for his valuable support and guidance during the thesis work, which helped me to develop a wider point of view and for sharing his knowledge and experience with me. It was a great chance to work with him.

I want to thank my thesis committee members Prof. Dr. Oğuz Uzol and Prof. Dr. Zafer Dursunkaya for their recommendations and advice that contributed significantly to the thesis.

Special thanks go to my friends Kenan Cengiz, Özgür Harputlu, Özgür Yalçın, H. Berk Gür, Ömer Ataş, A. Hazal Altuğ Yalçın, Metehan Yayla, Arda Akay, Engin Leblebici, Derya Kaya, Tansu Sevine, Tuğba Tuncel and H. Levent Şahin for their moral support during the successful completion of this thesis. It was a wonderful journey with them. Besides, I want to express my deepest thanks to my colleagues and staff in the Aerospace Engineering.

Last but not least, I would like to thank my parents and my sister for their care and support.

The support of TUBİTAK-BİDEB PhD scholarship (2211-C) program is gratefully acknowledged.

## TABLE OF CONTENTS

ABSTRACT . . . . .	v
ÖZ . . . . .	vii
ACKNOWLEDGMENTS . . . . .	x
TABLE OF CONTENTS . . . . .	xi
LIST OF TABLES . . . . .	xv
LIST OF FIGURES . . . . .	xvi
LIST OF ABBREVIATIONS . . . . .	xx
CHAPTERS	
1 INTRODUCTION . . . . .	1
1.1 Atmospheric Icing . . . . .	2
1.2 Parameters Affecting Icing . . . . .	4
1.2.1 Liquid Water Content (LWC) . . . . .	4
1.2.2 Median Volumetric Diameter (MVD) . . . . .	4
1.2.3 Wind Speed . . . . .	4
1.2.4 Temperature . . . . .	5
1.2.5 Blade Size . . . . .	5
1.3 Effects of Icing on Wind Turbines . . . . .	6
1.3.1 Full Stop of the Turbine . . . . .	6

1.3.2	Aerodynamic Performance Degradation . . . . .	6
1.3.3	Mechanical Failures . . . . .	7
1.3.4	Measurement Errors . . . . .	7
1.3.5	Increase in Noise Levels . . . . .	7
1.3.6	Overloading Due to Delayed Stall . . . . .	7
1.3.7	Safety Hazard . . . . .	8
1.4	ADIS Systems on HAWT . . . . .	8
1.5	Literature Review . . . . .	9
1.5.1	Ice Accretion Modeling Studies in Literature . . . . .	10
1.5.2	Ice Induced Performance Losses in Wind Turbines . . . . .	11
1.6	Objectives . . . . .	13
1.7	Thesis Outline . . . . .	14
2	METHODOLOGY . . . . .	15
2.1	Ice Accretion Prediction Tool . . . . .	15
2.1.1	Flow Field Solution: Hess-Smith Panel Method . . . . .	16
2.1.2	Droplet Trajectories and Collection Efficiencies . . . . .	17
2.1.3	Thermodynamic Analysis . . . . .	19
2.1.4	Ice Accretion: Extended Messinger Model . . . . .	21
2.1.5	Multi-layer Calculation Approach and Smoothing Algorithm . . . . .	23
2.1.6	Error Analysis for Predicted Ice Shapes . . . . .	24
2.2	Blade Element Momentum Theory . . . . .	25
2.2.1	Blade Element Theory . . . . .	26

2.2.2	Method Used in This Study . . . . .	27
2.2.3	Algorithm of the BEM Theory . . . . .	30
2.3	Coupling BEM Theory with Ice Accretion Prediction Tool . .	30
2.4	Gradient Based Aerodynamic Shape Optimization . . . . .	31
3	RESULTS AND DISCUSSION . . . . .	35
3.1	Validation Cases for Ice Accretion Prediction . . . . .	35
3.1.1	Effect of Droplet Size and Temperature on Icing . .	40
3.2	Validation of Power Production Predictions . . . . .	43
3.2.1	Verification of XFOIL Predictions for an Iced Blade Profile . . . . .	43
3.2.2	Validation of the BEM Tool . . . . .	47
3.3	Power Production Losses due to Icing . . . . .	48
3.3.1	Aeolos-H 30kW wind turbine . . . . .	48
3.3.2	NREL 5MW wind turbine . . . . .	57
3.4	Aerodynamic Shape Optimization to Reduce Power Losses due to Icing . . . . .	58
4	CONCLUSION . . . . .	65
	REFERENCES . . . . .	67
A	ICING SEVERITY . . . . .	73
B	AERODYNAMIC STALL . . . . .	75
B.1	Static Stall . . . . .	75
B.2	Dynamic Stall . . . . .	76
B.2.1	Stall Delay . . . . .	76
B.2.2	Overshoot of the Lift Force . . . . .	76

CURRICULUM VITAE ..... 77

## LIST OF TABLES

### TABLES

Table 1.1	Comparison of wind turbine and aircraft icing [1]. . . . .	2
Table 1.2	Available ADIS systems on commercial wind turbines [2, 3]. . . . .	9
Table 3.1	Atmospheric icing conditions (Blade profile=S809, Chord=0.267 <i>m</i> , Ambient pressure=95610 Pa, Humidity=100%). . . . .	36
Table 3.2	Percent error in predicted ice volume for S809 blade profile. . . . .	39
Table 3.3	Atmospheric icing conditions. . . . .	39
Table 3.4	Percent error in predicted ice volume for DU 93-W-210 blade profile. . . . .	42
Table 3.5	Geometric characteristics and flow conditions used in the calculations. . . . .	42
Table 3.6	Geometric characteristics of NREL phase II wind turbine. . . . .	47
Table 3.7	Parameters used to define icing profiles. . . . .	49
Table 3.8	Properties of NREL 5 <i>MW</i> wind turbine and atmospheric icing con- ditions. . . . .	59
Table A.1	IEA ice classification with corresponding recommendations (Reprinted from Ref [4]. . . . .	74

## LIST OF FIGURES

### FIGURES

Figure 1.1	Rime, Glime, Glaze [5] and Beak [6] type ice shapes. . . . .	3
Figure 1.2	Median volumetric diameter effect on trajectories. . . . .	5
Figure 1.3	De-icing of turbine blades [7]. . . . .	8
Figure 1.4	Temperature induced parasite drag penalty for NACA 0012 airfoil [8].	11
Figure 1.5	Ice load distribution at different wind and rotational speeds [9]. . .	12
Figure 1.6	Percent loss of power production because of the ice accumulation as a function of freestream wind speed [10]. . . . .	13
Figure 1.7	Power measurements at Gütsch and the bin-averaged power curve compared to the manufacturer's power curve [11]. . . . .	14
Figure 2.1	Definition of collection efficiency. . . . .	19
Figure 2.2	Smoothing without shrinkage. . . . .	24
Figure 2.3	Geometrical illustration for the cumulative error [12]. . . . .	25
Figure 2.4	The Blade Element Model. . . . .	27
Figure 2.5	Velocity triangle for a blade element. . . . .	28
Figure 2.6	Flowchart of the algorithm of BEM Theory. . . . .	31
Figure 2.7	Hicks-Henne bump functions (top) and its effect on a baseline air- foil (bottom). . . . .	33

Figure 2.8	Flowchart of Methodology. . . . .	33
Figure 3.1	Predicted ice shapes for S809 blade profile for conditions in Table 3.1 for AERTS case 16 [13]. . . . .	37
Figure 3.2	Predicted ice shapes for S809 blade profile for conditions in Table 3.1 for AERTS case 17 [13]. . . . .	38
Figure 3.3	Predicted ice shapes for S809 blade profile for conditions in Table 3.1 for AERTS case 24 [13]. . . . .	38
Figure 3.4	Predicted ice shapes for DU 93-W-210 for conditions given in Ta- ble 3.3. . . . .	40
Figure 3.5	Predicted ice profiles for NACA 64618 airfoil for conditions in Table 3.5 . . . . .	41
Figure 3.6	Predicted ice profiles for NACA 0012 airfoil for conditions in Table 3.5. . . . .	41
Figure 3.7	Clean and iced DU93-W210 blade profiles. . . . .	44
Figure 3.8	Computational mesh used for generating iced airfoil polars with 100k cells on a structured grid topology. . . . .	44
Figure 3.9	Flow fields and surface pressure distributions predicted by SU2 and XFOIL. . . . .	45
Figure 3.10	Aerodynamic coefficients of clean DU93-W-210 blade profile at $Re = 1.0 \times 10^6$ . . . . .	46
Figure 3.11	Aerodynamic coefficients of iced DU93-W-210 blade profile at $Re = 1.0 \times 10^6$ . . . . .	46
Figure 3.12	Experimental aerodynamic coefficients of S809 blade profile at $Re = 1.0 \times 10^6$ [14]. . . . .	48
Figure 3.13	Test data and simulations comparison for NREL Phase II wind turbine [14]. . . . .	49

Figure 3.14 Predicted ice profiles for icing conditions given in Table 3.7 at the rated wind speed of $11m/s$ and $45min$ exposure time. . . . .	50
Figure 3.15 Predicted ice shapes for conditions in Table 3.7 at the wind speed of $8.5m/s$ ( $LWC = 0.05g/m^3$ , $T_a = -10\text{ }^\circ\text{C}$ , $MVD = 27\mu m$ ). . . . .	52
Figure 3.16 Predicted ice shapes for conditions in Table 3.7 at the rated wind speed of $11m/s$ ( $LWC = 0.05g/m^3$ , $T_a = -10\text{ }^\circ\text{C}$ , $MVD = 27\mu m$ ). . . . .	53
Figure 3.17 Predicted ice shapes for conditions in Table 3.7 at the wind speed of $15m/s$ ( $LWC = 0.05g/m^3$ , $T_a = -10\text{ }^\circ\text{C}$ , $MVD = 27\mu m$ ). . . . .	54
Figure 3.18 Predicted ice profiles for icing conditions given in Table 3.7 at the rated wind speed of $11m/s$ and $45min$ exposure time. . . . .	55
Figure 3.19 Predicted ice profiles over the blade at rated wind speed and power curve for $45min$ exposure time. . . . .	56
Figure 3.20 Predicted ice profiles over the blade and sectional power production at rated wind speed. . . . .	57
Figure 3.21 Predicted power production and percent power loss for various icing exposure times. . . . .	58
Figure 3.22 Predicted ice shapes at $10\text{ }m/s$ for NREL $5MW$ wind turbine under icing conditions in Table 3.8. . . . .	59
Figure 3.23 Predicted ice shapes for conditions in Table 3.8 at the wind speed of $10m/s$ . . . . .	60
Figure 3.24 Bump functions (left), Aeolos wind turbine baseline blade profile (DU93-W-210) and the optimized profile (right). . . . .	61
Figure 3.25 Predicted ice profiles for baseline and optimized blade profiles at rated wind speed ( $LWC=0.05g/m^3$ , $MVD=18\mu m$ , $T_a=-10\text{ }^\circ\text{C}$ ). . . . .	62
Figure 3.26 Power production of Aeolos $30\text{ kW}$ wind turbine. . . . .	63
Figure A.1 Definition of the icing event. . . . .	73

Figure B.1 A representative schematic diagram of lift under static and dynamic changes in the angle of attack. . . . .	75
Figure B.2 A typical hysteresis loop for a wind turbine blade profile [3]. . . . .	76

## LIST OF ABBREVIATIONS

### ACRONYMS

<i>ADIS</i>	Anti-icing and De-icing Systems
<i>AEP</i>	Annual Energy Production
<i>BEM</i>	Blade Element Momentum
<i>CC</i>	Cold Climate
<i>CFD</i>	Computational Fluid Dynamics
<i>CW</i>	Cold Weather
<i>FAR</i>	Federal Aviation Regulation
<i>HAWT</i>	Horizontal Axis Wind Turbine
<i>IEA</i>	International Energy Agency
<i>LWC</i>	Liquid Water Content
<i>MVD</i>	Median Volumetric Diameter
<i>SCADA</i>	Supervisory Control and Data Acquisition
<i>WECS</i>	Wind Energy Converting System

### ROMAN SYMBOLS

<i>a</i>	Axial Induction Factor
<i>a'</i>	Angular Induction Factor
<i>c</i>	Chord length of the airfoil
<i>C<sub>f</sub></i>	Skin friction
<i>F<sub>x</sub></i>	Axial force
<i>F<sub>θ</sub></i>	Tangential force
<i>g</i>	Gravitational acceleration
<i>h</i>	Water film height
<i>h<sub>t</sub></i>	Heat transfer coefficient

$k_s$	Roughness height
$M$	Mach Number
$N$	Number of blade elements
$P_r$	Laminar Prandtl number of air
$P_{rt}$	Turbulent Prandtl number of air
$R$	Blade tip radius
$Re$	Reynolds number
$Re_k$	Roughness Reynolds number
$RH$	Relative humidity
$r$	Radius and radial direction
$Sc$	Schmidt number
$St$	Stokes number
$Sta$	Stanton number
$T$	Torque
$t$	Time
$U_e$	Flow velocity at the boundary-layer edge
$U_k$	Flow velocity at the roughness location
$u, v$	Cartesian Velocities in x and y directions
$x, y$	Rectangular Cartesian Coordinates
$x_p, y_p$	Position vector components of the cloud particle
$\dot{x}_p, \dot{y}_p$	Velocity vector components of the cloud particle
$\ddot{x}_p, \ddot{y}_p$	Acceleration vector components of the cloud particle

### **GREEK SYMBOLS**

$\alpha$	Angle of attack
$\beta$	Blade Twist Angle
$\gamma$	Airfoil inlet angle
$\gamma$	Turbin twist angle

$\delta$	Thickness of boundary layer
$\lambda$	Tip speed ratio
$\mu$	Dynamic viscosity
$\nu$	Kinematic viscosity
$\rho$	Density of air
$\rho_r$	Density of rime ice
$\rho_g$	Density of glaze ice
$\sigma_w$	Surface tension of water
$\sigma'$	Local solidity
$\tau$	Shear stress
$\lambda_r$	Local Tip speed ratio
$\Omega$	Blade rotational speed
$\omega$	Wake rotational speed

### **Subscripts and Superscripts**

$()_a$	Ambient properties
$()_f$	Freeze properties
$()_i$	Ice properties
$()_k$	Airflow properties at roughness height
$()_p$	Particle properties
$()_w$	Water properties

## **CHAPTER 1**

### **INTRODUCTION**

In recent years, energy production from renewable energy sources is in great demand and installation of wind turbines in the world has been increasing in a steady manner. Currently, about 3% of the world's electricity is produced by wind power and this share is expected to double by the end of 2018 [15].

Wind farms in cold climate regions and highlands have the advantage of high wind speeds, high air density and sparsely populated residential areas. However, especially in winter, the wind turbines are subjected to severe atmospheric icing conditions, which have a detrimental effect on both the operation and performance of the wind turbine. Formation of ice on wind turbine blades creates various undesired consequences such as aerodynamic performance loss by changing blade aerodynamic characteristics and reduction of the lifetime of the components on wind turbines. In horizontal axis wind turbines, aerodynamic performance losses are similar to those observed in wings and helicopter rotors under icing conditions [16]. The similarities and differences between wind turbine and aircraft icing can be seen in Table 1.1.

Increase in the amount of power production loss depends on the kind of ice which shape develops on blades, and the duration of icing [17, 18]. In order to maximize energy production from the turbine which is operating under icing conditions, that predict ice formation on turbine blades can help maintain safety, reduce performance losses and decrease weight. Minimization of ice accumulation on wind turbine blades is therefore needed for reducing performance losses and maintaining safety.

Table 1.1: Comparison of wind turbine and aircraft icing [1].

	Wind turbine	Aircraft
General	Unavoidable, gradual, long, remote	Sudden, fatal, short, expensive
Ice accumulation	Leading edge and other parts of turbine	Leading edge
Icing phenomena	Freezing rain, drizzle, 0-250m, Turbulent shear boundary layer	SLD, ice crystal, 0-12km, Uniform freestream
Exposure time	Days	45, 30, 23 minutes
Iced surface	Fatigue	Vibration due to asymmetric ice accretion
Anti/de-ice	Hot-air, electro thermal, boot, natural using centrifugal force, black paint	Boot, hot-air, Retrofittable
Life time	15-20 years	30 years
Instrument	Anemometer/wane vane malfunction	Pitot tube malfunction

## 1.1 Atmospheric Icing

It is well-known that icing occurs when supercooled water droplets in the atmosphere impinge on a surface such as a turbine blade. Temperature, liquid water content (LWC), median volumetric diameter (MVD), airspeed and geometry size are the basic factors affecting icing. Temperature influences the type and intensity of ice. Liquid water content determines the severity of icing, type and shape. Median volumetric diameter indicates the type and rate of icing. The blade size determines the rate of ice accretion. The different classes of accreted ice vary in their shape, color, density, adhesion and cohesion properties. Supercooled water droplets may freeze instantly and form rime ice on the surface or run downstream on the blade surface and freeze later forming glaze ice structures.

Rime, glaze and mixed (glime) ice are three types of ice formation seen in atmospheric conditions. Rime ice typically forms at temperatures from 0 °C down to -40 °C. This kind of ice has a milky, opaque appearance with smooth shapes, tends to grow into the air-stream, and can be easily removed by de-icing or prevented by anti-icing systems. It usually occurs at low airspeed, low temperature and low liq-

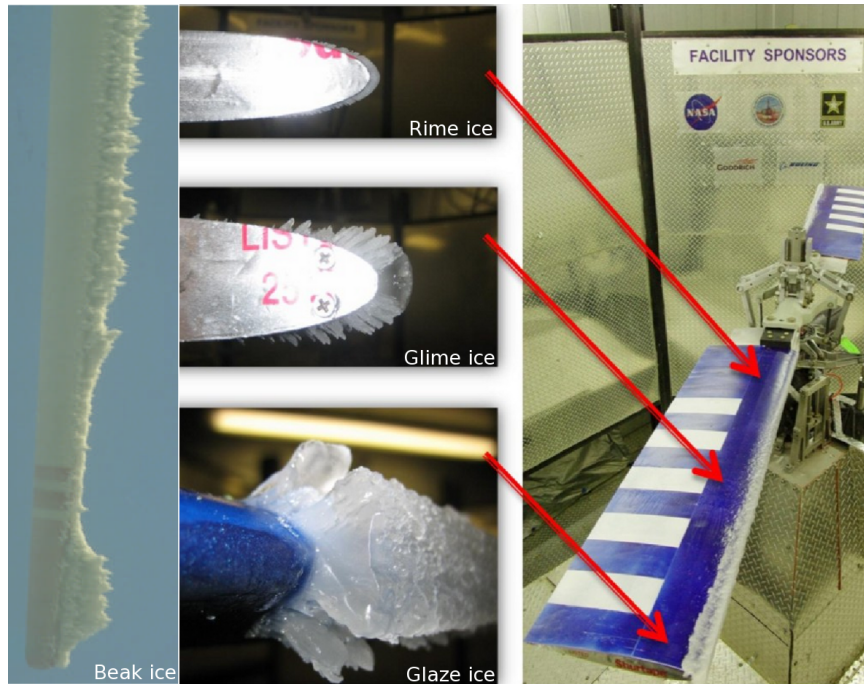


Figure 1.1: Rime, Glime, Glaze [5] and Beak [6] type ice shapes.

uid water content. Glaze ice occurs at temperatures between 0 and  $-6$  °C. Glaze ice has a transparent appearance with irregular shapes like horns and is hard to remove by de-icing systems. It occurs at high airspeed, high temperature and high liquid water content when a fraction of the water droplets freeze upon impact while remaining droplets run along the surface and freeze downstream. Density of glaze ice ( $900\text{kg}/\text{m}^3$ ) is greater than that of rime ice ( $200 - 800\text{kg}/\text{m}^3$ ) and creates higher ice loads on turbine blades. Mixed ice is a combination of rime and glaze ice. It occurs in layers from rime to glaze ice. Due to variation in the sectional velocity and angle of attack with span along the turbine blade, it is possible that both rime and glaze ice forms at different radial positions on the blade. In addition to this, a special icing type called beak ice [19] is formed on the tip sections of the turbine blade. Beak ice is observed during operation of rotary machines such as in wind turbine blades, when some part of the accreted ice breaks and sheds due to centrifugal and torque bending forces. Beak ice looks like a saw tooth and all four kinds of ice are illustrated in Figure 1.1.

## **1.2 Parameters Affecting Icing**

Atmospheric conditions such as liquid water content, median volumetric diameter and wind speed significantly affect ice accretion on wind turbine blades.

### **1.2.1 Liquid Water Content (LWC)**

It is the amount of the mass of the water in a medium (cloud, fog, ie.) in a specified volume of dry air. Higher LWC denotes more water in the air. It depends on the type of the clouds and exposure distances for a given temperature and droplet size which are presented in FAR/CS 25 Appendix C. LWC has an impact on both the rate and type of ice accretion. In terms of the ice formation process, LWC affects the type and size of the ice at which the accretion may occur. For the same icing conditions, as the LWC becomes higher the required latent heat which must be removed from the incoming impinging droplets to freeze completely also becomes large, and therefore the tendency of ice formation is in favor of glaze ice.

### **1.2.2 Median Volumetric Diameter (MVD)**

Median volumetric diameter of liquid water droplets is a property that indicates the average water droplet size in an icing cloud or fog. The airflow around a turbine blade or wing deflects the particles to some extent, which potentially impact the surface. Smaller droplets are more easily deflected by the airflow than larger droplets due to their lower kinetic energy and since the kinetic energy of droplets grows as the droplet size increases and larger droplets pursue ballistic-like trajectories as illustrated in Figure 1.2. As a consequence of this, collection efficiency grows significantly as the droplet size becomes larger and the impingement zone gets wider.

### **1.2.3 Wind Speed**

Wind speed is another factor affecting ice formation. As speed increases, droplets follow ballistic-like trajectories since they do not have sufficient time to deviate from the

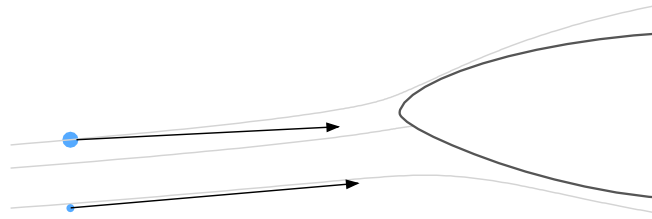


Figure 1.2: Median volumetric diameter effect on trajectories.

surface. Therefore, more droplets hit the surface which results in a wider impingement region and consequently more ice accretion. Moreover, aerodynamic heating causes the ice type accreted on the surface to change. For the rotary blades, the local speed of the sectional blade varies with radial location, therefore different kinds of ice can be formed at different radial positions on the blade.

#### 1.2.4 Temperature

Temperature has an important influence on icing in terms of amount of accreted ice, its type and shape. Small differences in the temperature may result in totally different kinds of ice. During ice formation process the ambient temperature governs the convective cooling of incoming water droplets. Besides, there is a secondary effect of temperature which is related to liquid water content. The lower the ambient temperature, the less the heat contained in the atmosphere, hence the atmosphere can hold more water vapor.

#### 1.2.5 Blade Size

Large turbine blades create a greater obstacle for incoming droplets, and drive droplets to deviate significantly away from them. Therefore, the droplet trajectories pursue the streamlines and less droplets impact the surface resulting in lower collection efficiencies and narrower impingement zones. In other words, the smaller chord length, the more prone the wing is to icing for the same icing conditions.

### **1.3 Effects of Icing on Wind Turbines**

Wind turbines located in highlands and cold climates confront icing related problems over their service life and some of these unwanted issues are discussed in the following sections.

#### **1.3.1 Full Stop of the Turbine**

Sometimes, heavy icing may result in the total shutdown of the turbine. Ice accumulation along the turbine blades creates aerodynamic imbalances, which produces additional vibrations by changing the mass center of the turbine blades. Before these vibrations reach the natural frequency the turbine should be forced to stop to prevent structural failures. Two examples to this were observed in the winter of 2002-2003 at Äppelbo in Sweden and in the winter of 2010 at New Brunswick, Canada. While at Äppelbo a 900 kW NEG-micron wind turbine was stopped due to icing for 7 weeks [20], the wind turbines, located 70 kilometers northwest of Bathurst, New Brunswick were completely out of order for several weeks because of the heavy ice covering the turbine blades [21]. Total downtime for wind farms can lead to significant energy losses.

#### **1.3.2 Aerodynamic Performance Degradation**

Ice formation on the turbine blades alters the original shape and this causes changes in the aerodynamic characteristics of the blade. Ice induced roughness leads to an increase in the drag coefficient and decrease in the lift coefficient and may even cause premature flow separation on the turbine blades. This aerodynamic performance degradation can reduce the power coefficient in the range of 20–50% [22] and the annual power losses can reach to 50% [23] at sites with harsh conditions.

### **1.3.3 Mechanical Failures**

Ice accretion over the rotating blade builds up mostly on the leading edge of the blade and can cause critical unbalanced loads on the wind turbine. These loads cause high amplitude vibrations at the blades and result in increased material fatigue, bringing down the operational life of the turbine. Additionally, operation at low temperatures influences oil viscosity and alters the mechanical properties of different components of the wind turbine. As a result of these circumstances overheating takes place in the gearbox.

### **1.3.4 Measurement Errors**

In atmospheric icing conditions, the anemometers, wind vanes and temperature sensors are affected by ice formation. Ice-induced measurement errors from turbine instruments may affect yaw and power controls. During an icing event, the measurement errors for wind speed can reach up to 30% [24]. In a different study, Fortin et al. [25] reported an uttermost error of 60% for a standard anemometer and 40% for an ice free anemometer.

### **1.3.5 Increase in Noise Levels**

The noise level generated by the wind turbine increases when the turbine blade is iced, and mostly, the blade noise emission frequency is shifted to higher frequencies, since any kind of ice formation on the leading edge of a turbine blade forces a transition from laminar flow regime to the turbulent flow, hence increased frequency noise.

### **1.3.6 Overloading Due to Delayed Stall**

Rime ice accretion acts as a leading edge flap and delays aerodynamic stall to a higher angle of attack. Although this leads to a higher energy production, more loads are generated on the blades, and this additional energy production can damage the electrical components of the turbine.



Figure 1.3: De-icing of turbine blades [7].

### 1.3.7 Safety Hazard

Ice thrown from rotating turbine blades may cause danger both for humans and other wind turbines in the vicinity. Although the risks are greatest for maintenance crew, others can be at danger near a road in case the wind farm is located near a rural area.

## 1.4 ADIS Systems on HAWT

In spite of all these detrimental effects of icing on wind turbine blades, cold climate regions attract the attention of the investors since air density variations affect the power production and there is much denser air in cold regions than warm regions. Accordingly, to utilize the high energy potential of cold regions, active or passive anti/de icing systems (ADIS) can be used in the wind turbines to prevent or mitigate icing as in the case of aircraft icing, Figure 1.3.

Table 1.2 provides a list of available ADIS systems for the main wind turbine manufacturers. For anti-icing the main goal is to prevent ice accretion (e.g. hydrophobic coating with black painting), while in the case of de-icing a limited amount of ice layer is allowed to grow before being removed from the surface (e.g. heating). System power requirements and the blade rotation make the implementation of ADIS systems on wind turbines more difficult than air vehicles [26]. A critical review study about ADIS usage in wind turbines is undertaken by Parent and Ilinca [27]. It is stated that electro-thermal and hot air flow systems are generally used in ADIS, hence wind

turbines require more energy to operate. Although early power consumptions of electrical heating were  $\approx 25\%$  of the nominal power output of the given turbine, with the advances in technology this consumption is reduced to  $\approx 2\%$  of nominal power output. Nowadays ADIS use up 4% of the annual energy production depending on the severity of icing. Icing simulations can help in the positioning of ADIS for reducing energy consumption necessitated to operate these devices.

Table 1.2: Available ADIS systems on commercial wind turbines [2, 3].

<b>Manufacturer</b>	<b>Type of ADIS system (% of year)</b>
Acciona	Hot air
Adios	Electro-thermal (third party)
Alstom	Hot air
Dongfang	Hot air and electro-thermal
Enercon	Hot air
GreenWindGlobal (ECO Temp)	Electro-thermal (third party)
Gamesa	Hot air/electro-thermal/coating
Kelly-Aerospace	Electro-thermal (third party)
Leitwind	Electro-thermal
Nordex	Electro-thermal
REpower	coating
Senvion	Hot air
Siemens	Electro-thermal
Vestas	Hot air/electro-thermal
WiceTec (VTT)	Electro-thermal (third party)
WinWinD	Electro-thermal

## 1.5 Literature Review

Icing is a natural phenomenon which creates undesired and critical issues on high voltage wires, aircraft and wind turbines. Therefore, physics of icing is an object of interest, which stands as a challenge for the scientists and still continue to be a hot topic in the literature. Previous studies about icing are given in two subsections below. While in the first subsection information about icing modeling and its evolution is given, in the second subsection some information about wind turbine icing related studies are discussed.

### 1.5.1 Ice Accretion Modeling Studies in Literature

Ice accretion and its effects on aircraft wings and control surfaces have been studied by many researchers and well documented by using climatic wind tunnels and numerical simulation. For the first time in the literature, in 1953 Messinger [28] introduced an analytical model to predict ice accretion on an unheated surface by using mass and energy balance equations, but study of the Myers [29] is a milestone research in icing modeling, because it presents the Extended Messinger Model, which has been used by a large number of icing simulation tools since its introduction. With this extension, mathematical models for glaze ice and rime ice are identified, and 1-D model that is defined is also extended to two and three dimensions. Özgen and Canbek [30] used the Extended Messinger Model to predict ice shapes on a multi-element airfoil in two-dimensions and compared the obtained results with both experimental and numerical data. Besides, effects of chord length, wind speed, angle of attack, liquid water content and droplet diameter on collection efficiency are investigated.

Lynch and Khodadoust [8] prepared an extensive literature review study about the aerodynamic performance and control degradation caused by icing on aircraft wing profiles. Available research about maximum lift reductions, stall angle reductions and drag penalties reported in the literature are given in detail both for in-flight and ground ice accretions. One of the critical results about drag increase is depicted in Figure 1.4.

Numerical simulations are conducted over clean and iced wind turbine blade profiles for various angles of attack. It is seen that ice accretion adversely affects the lift and drag coefficients [16, 31]. Ibrahim et al. [32] studied the ice shapes on 35 different NREL airfoils and aerodynamic loads on NREL S809 airfoil for different icing events. According to the results, maximum airfoil thickness and its location from the leading edge has great impact on icing. Besides, the loss in lift coefficient due to icing calculated up to 65% depending on ice shape.

Fu et al. [9] predicted icing loads on NREL phase VI turbine blade for different wind and rotation speeds. It is concluded that ice is formed mainly at the leading edge and

Symbol	V (km / hr)	M <sub>0</sub>	LWC (g/m <sup>3</sup> )	MVD (μm)	Duration (minutes)	RN <sub>c</sub> x 10 <sup>-6</sup>
○	209	0.18	1.3	20	8	2.3 – 2.8
□	338	0.29	1.05	20	6.2	3.7 – 4.5

Note: LWC x V x Duration = constant

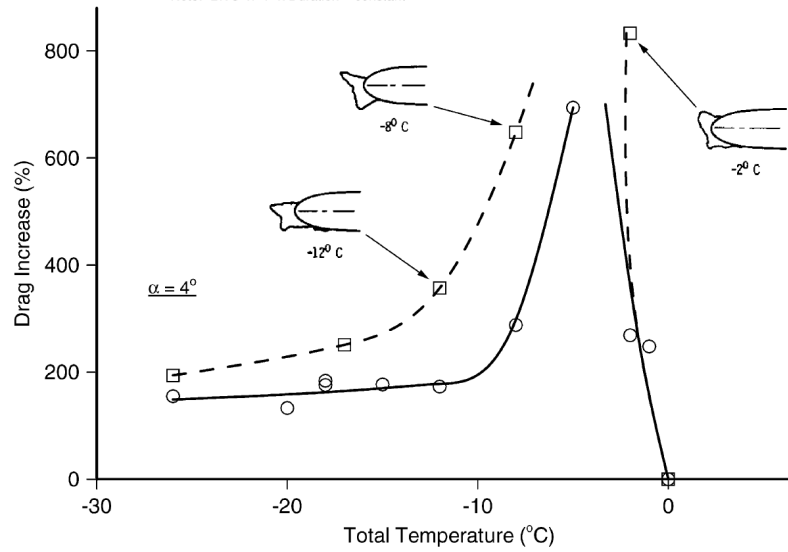


Figure 1.4: Temperature induced parasite drag penalty for NACA 0012 airfoil [8].

tip of the blade, and as the wind or rotational speed increases mass of the accumulated ice increases, as it is presented in Figure 1.5.

Some of the previous studies investigate the ice accretion prediction on rotor system by calculating performance degradation and analyzing shedding by coupling the Blade Element Momentum Theory (BEMT) model with LEWICE ice shape prediction tool [33]. However, performance degradation of iced blade is predicted by using empirical ice performance equations based on the clean airfoil performance.

### 1.5.2 Ice Induced Performance Losses in Wind Turbines

Wind power estimation plays an important role on wind farm assessment process. Especially for cold climate regions, the effect of icing on rotor aerodynamics should be reconsidered since 10–15% of the system capital cost is the wind turbine blade cost [34]. Therefore, experimental and computational studies are performed to examine performance losses due to icing.

Prediction of ice accretion on wind turbine blades and its effect on turbine perfor-

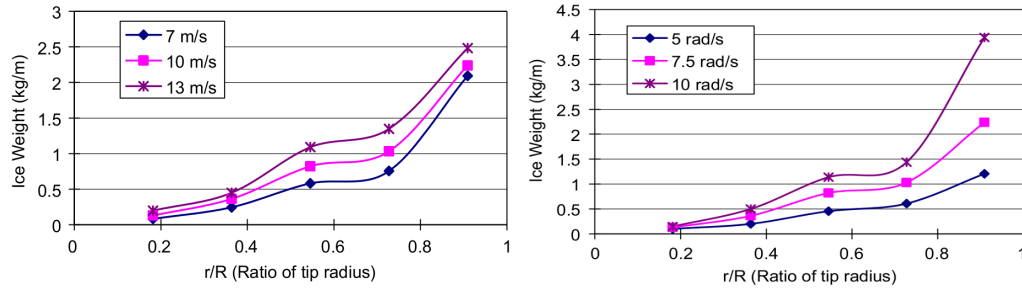


Figure 1.5: Ice load distribution at different wind and rotational speeds [9].

mance is a challenge because of the uncertainty in the parameters such as liquid water content, temperature, wind speed and turbulent gust. Neglecting these uncertainties by using constant parameters in numerical modeling leads to significant difference between predicted and real ice shapes especially in glaze and beak ice conditions. There are experimental, statistical and numerical studies in the literature that investigate icing effects on wind turbines. Scientists carry out wind tunnel tests under clean and different icing conditions to predict the degradation in wind turbine performance. Experimental methods are expensive in the climatic wind tunnels and mainly used only for validation. Generally in experimental studies, wind tunnel tests are performed using artificial ice profiles on turbine blades to estimate turbine performance losses [35, 36].

Reid et al. [10] studied performance degradation of the NREL phase VI wind turbine for four different icing events with one hour exposure time. According to the results in Figure 1.6, the performance loss of the simulated NREL phase VI turbine can reach above 60%.

Numerical studies [37, 38, 39], which are carried out for various turbine blade profiles under similar constant icing conditions predict power losses in the 20–35% range. This power production loss reported in the literature is in good agreement with the observations from wind farms of Site A [40] and Site 1-2 [41]. Site A exposes light and moderate icing about 10% of the year and measured data for four winters showed 24% production loss. Based on four years of operational data recorded by the SCADA system of the wind turbines analyzed for Site 1 and Site 2, it is stated that 23 icing events lasting 308 hours on Site 1 and 19 icing events lasting 213 hours on Site 2

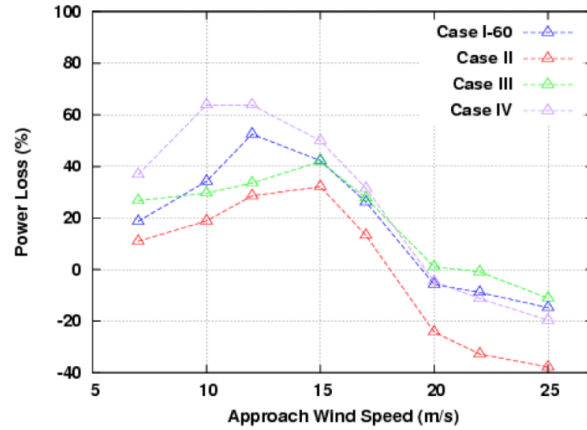


Figure 1.6: Percent loss of power production because of the ice accumulation as a function of freestream wind speed [10].

ended up with an average 26% and 27% production loss, respectively. Besides in cold climate regions, icing can result in up to 17% loss in Annual Energy Production (AEP) and reduce the power coefficient in the range of 20–50% [42, 22]. Although an AEP loss as high as 23% (reduction from 986 MWh to 785 MWh) based on the measured data at the Alpine Test Site Güttsch is reported, Barber et al. [11] explain this large loss by including the high turbulence and the wind gust related losses as an additional factor into the icing losses. Power curve of the Güttsch turbine is shown in Figure 1.7.

It should be noted that the power loss heavily depends on the icing severity due to liquid water content, droplet diameter and icing exposure time.

## 1.6 Objectives

The main objectives of the present study are :

- To develop a cost-effective tool for the prediction of ice accretion on wind turbine blades under various atmospheric icing conditions
- To estimate power production losses due to icing
- To develop a gradient based shape optimization tool to maximize the power

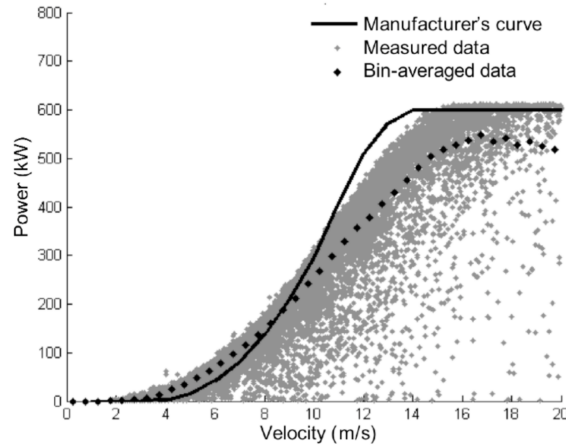


Figure 1.7: Power measurements at Gütsch and the bin-averaged power curve compared to the manufacturer's power curve [11].

production under icing conditions by modifying the baseline blade profile

## 1.7 Thesis Outline

This thesis is divided into three remaining chapters to cover the objectives properly.

In Chapter 2, the ice accretion methodology based on the Extended Messinger Model is introduced. The Blade Element Momentum (BEM) methodology applied for ice induced performance losses on wind turbines is then described in detail.

In Chapter 3, the numerical results of predicted ice shapes on turbine blades and related performance losses on wind turbines are presented and discussed. Initially, validation studies are carried out for icing simulations on various validation cases are presented. Then, performance analyses are performed for both clean and iced wind turbine blades to investigate ice related power losses. Lastly, blade profiles optimized by using a gradient based optimization algorithm and Hicks-Henne bump functions for reducing power production losses of iced wind turbines, are introduced.

Chapter 4 summarizes significant results of the study and states suggestions for future work.

## CHAPTER 2

### METHODOLOGY

In this study, an efficient ice accretion prediction tool coupled with the Blade Element Momentum (BEM) method is developed in order to predict ice shapes on wind turbine blades and related power production losses. In addition, a gradient based shape optimization algorithm is developed to reduce the ice accumulation on wind turbine blades and to minimize the power production losses. The BEM tool employs the 2D potential flow solver with viscous effects, XFOIL [43].

The ice accretion prediction tool predicts the ice shapes of the sectional blade profiles for a given set of atmospheric icing conditions. XFOIL then supplies the sectional aerodynamic loads including viscous effects for clean and iced blade profiles under the local flow conditions. The numerical method is comprised of three main modules, which are explained below in detail.

#### 2.1 Ice Accretion Prediction Tool

Ice accretion modeling made it possible to acquire numerical data for creating ice shapes from aircraft wings to the transmission line wires under a wide range of icing conditions. In the current study, icing module is used to predict the sectional ice shapes on a wind turbine blade. The main inputs to this module are blade section geometry, flow conditions (free stream velocity, angle of attack, etc.) and meteorological conditions (temperature, liquid water content (LWC), median volumetric diameter (MVD), exposure time, etc.). The main outputs are sectional ice shape geometry and corresponding aerodynamic coefficients.

Ice accretion prediction involves complex physics comprising aerodynamics, heat transfer and multiphase flow, which are all time dependent and involve geometric deformation. Some assumptions and simplifications are needed to obtain a numerical solution. Ice accretion models work well for the prediction of water catch rates and collection efficiencies. The numerical method employed in this study predicts the ice accretion on aerodynamic surfaces as a result of supercooled water droplets hitting the surface. It employs the general methodology for the simulation of ice accretion on airfoils, which is based on the successive calculation of air flow, water droplet trajectories, collection efficiency, heat transfer balance and accreted ice in an iterative manner. In order to determine the flow field velocity components for droplet trajectory calculations, a panel method is used. Droplet trajectories are computed by using a Lagrangian approach to obtain the collection efficiency distribution around the airfoil. To determine the ice thickness in the direction normal to the surface, the distribution of convective heat transfer coefficient is determined by using the two-dimensional Integral Boundary Layer equation. The thermodynamic balance is then achieved with the Extended Messinger model.

Ice accretion modeling mainly consists of four steps: flow field solution; droplet trajectory calculations; thermodynamic analysis; and ice accretion simulation with the Extended Messinger Model. The numerical method is an iterative process with a time-stepping procedure, where ice accretion starts on the surface, followed by flow field and droplet trajectories recomputations.

### **2.1.1 Flow Field Solution: Hess-Smith Panel Method**

The flow field calculation is required to find the velocity of air at any point in the flow field to calculate droplet trajectories. In this study, 2-D Hess-Smith Panel Method is utilized for this purpose. The surface velocity distribution is also obtained through this solution, which is used in boundary layer calculations to evaluate the distribution of the surface convective heat transfer coefficient. A transition modeling is also employed in the solution of integral boundary layer equations.

Ice thicknesses obtained by solving the 1D conservation equations in the direction normal to the leading edge panels may produce highly oscillatory, jagged ice pro-

files. Since the panel method is quite sensitive to sharp variations in panel angles, ice profiles obtained are smoothed.

## 2.1.2 Droplet Trajectories and Collection Efficiencies

Ice accretion on blade surfaces depends on droplet trajectories and the resulting collection efficiency distribution. The droplet equation of motion is solved by using a Lagrangian approach to determine the droplet trajectories. The following assumptions are made:

- the droplets are of small size, i.e.  $MVD \leq 500 \mu m$
- the droplets are spherical
- the droplets are not deformable
- there is no coalescence or clash between droplets
- the water droplet concentration is small enough so that droplets have no effect on the flow analysis
- the only forces acting on the droplet are aerodynamic drag, gravity and buoyancy
- the droplets are supposed to have the same temperature as the flow

In the Lagrangian approach, individual water droplets are tracked from a specified far field location towards the body. Droplet trajectories are based on the following equations of motion:

$$m\ddot{x}_p = -D \cos \gamma \quad (2.1)$$

$$m\ddot{y}_p = -D \sin \gamma + mg \quad (2.2)$$

where

$$\gamma = \tan^{-1} \frac{\dot{y}_p - V_y}{\dot{x}_p - V_x} \quad (2.3)$$

$$D = \frac{1}{2} \rho V_{rel}^2 C_D A_p \quad (2.4)$$

$$V_{rel} = \sqrt{(\dot{x}_p - V_x)^2 + (\dot{y}_p - V_y)^2} \quad (2.5)$$

$V_x$  and  $V_y$  are the components of flow velocity at the droplet location, while  $\dot{x}_p$ ,  $\dot{y}_p$ ,  $\ddot{x}_p$  and  $\ddot{y}_p$  are the components of the droplet velocity and acceleration. The atmospheric density is denoted by  $\rho$ , while the droplet cross-sectional area and the drag coefficient are denoted by  $A_p$  and  $C_D$  respectively. The droplet drag coefficient is based on an empirical drag law as a function of the droplet Reynolds number. In the present study, the following formulation is employed for drag coefficients as Gent et al. [19] suggested.

$$C_D = \frac{Re}{24} \begin{cases} 1 + 0.197Re^{0.63} + 2.6 \times 10^{-4}Re^{1.38}, & \text{if } Re \leq 3500 \\ (1.699 \times 10^{-5})Re^{1.92}, & \text{if } Re > 3500 \end{cases} \quad (2.6)$$

$$Re = \frac{\rho d_p V_{rel}}{\mu} \quad (2.7)$$

In the above formulations,  $d_p$  is the droplet diameter,  $V_{rel}$  is the relative velocity of the particle and  $\mu$  is the dynamic viscosity. Sutherland viscosity law is used to calculate this parameter.

The droplet trajectories starting from upstream are then obtained by integrating the equations of motion in time until either a droplet impacts the blade surface or flows pass the blade. Initially, the droplet velocity is taken to be the terminal velocity given as follows:

$$V_{term}^2 = \frac{4(\rho_w - \rho)gd_p}{3\rho C_D} \quad (2.8)$$

The local collection efficiency ( $\beta$ ) indicating the probable iced region, is defined as the ratio of the area of impingement to the area through which water passes at some distance upstream of the section (Figure 2.1). This upstream distance is taken as 10 times of the chord length in the present study.

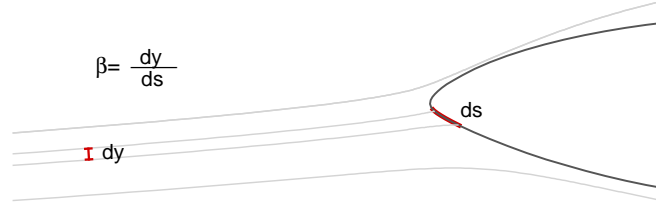


Figure 2.1: Definition of collection efficiency.

When the angle of attack is small, the local collection efficiency distribution generally has a peak in the vicinity of the stagnation point and reduces to zero at some point aft on the lower and upper blade surfaces.

### 2.1.3 Thermodynamic Analysis

The mass and energy balance at the blade surface are used to make thermodynamics analysis. To determine the thickness of ice, convective heat transfer coefficients are first determined by using the two-dimensional Integral Boundary Layer equation.

Initially, the transition point must be predicted since equations which are used for computing heat transfer coefficients depend on whether the flow is laminar or turbulent. Transition from laminar to turbulent flow occurs when the Reynolds number based on roughness height  $Re_k$  exceeds 600 which is defined as:

$$Re_k = \frac{\rho U_k k_s}{\mu} \quad (2.9)$$

where  $U_k$  is local flow velocity at the roughness height location and  $k_s$  is roughness height. Local flow velocity and roughness height are defined as :

$$\frac{U_k}{U_e} = 2\frac{k_s}{\delta} - 2\left(\frac{k_s}{\delta}\right)^3 + \left(\frac{k_s}{\delta}\right)^4 + \frac{1}{6}\frac{\delta^2}{v_a}\frac{dU_e}{ds}\frac{k_s}{\delta}\left(1 - \frac{k_s}{\delta}\right)^3 \quad (2.10)$$

$$k_s = \frac{4\sigma_w\mu_w}{\rho_w F \tau} \quad (2.11)$$

with  $\sigma_w$  being surface tension,  $\mu_w$  being viscosity of water,  $\rho_w$  is density of water,  $F$  is the fraction of blade section surface wetted by droplets and  $\tau$  is total shear stress. In addition,  $U_e$  is the flow velocity outside the boundary-layer at the roughness

location and  $s$  is the streamwise distance along the blade section surface starting at the stagnation point. The boundary layer thickness,  $\delta$  is [44]:

$$\delta = \frac{315}{37} \Theta_l \quad (2.12)$$

Thwaites formulation can be used for laminar momentum thickness computation as follows [44]:

$$\frac{\Theta_l^2}{\nu} = \frac{0.45}{U_e^6} \int_0^s U_e^5 ds \quad (2.13)$$

The convective heat transfer coefficients are calculated employing the methods of Smith and Spaulding relation in the laminar flow region and Kays and Crawford relation in the turbulent flow region [19].

$$h_c = \begin{cases} \frac{0.296kU_e^{1.435}}{\sqrt{\nu \int_0^s U_e^{1.87} ds}}, & \text{if } Re_k \leq 600 \\ St\rho U_e C_p, & \text{if } Re > 600 \end{cases} \quad (2.14)$$

$C_p$  is the specific heat of air and  $St$  is the Stanton number where [19]:

$$St = \frac{\frac{C_f}{2}}{Pr_t + \sqrt{\frac{(C_f/2)}{St_k}}} \quad (2.15)$$

Turbulent Prandtl number,  $Pr_t = 0.9$  and  $St_k$  is roughness Stanton number which is given as [19]:

$$St_k = 1.92Re_k^{-0.45}Pr_l^{-0.8} \quad (2.16)$$

Laminar Prandtl number,  $Pr_l = 0.72$ . Turbulent skin friction is given according to Makkanen relation as [19]:

$$\frac{C_f}{2} = \frac{0.1681}{[\ln(864\frac{\Theta_l}{k_s} + 2.568)]^2} \quad (2.17)$$

Turbulent momentum thickness is given as [19]:

$$\Theta_t = \frac{0.036\nu^{0.2}}{U_e^{3.29}} \left( \int_{s_{tr}}^s U_e^{3.86} ds \right) + \Theta_{tr} \quad (2.18)$$

$s_{tr}$  is transition location where  $Re_k = 600$  and  $\Theta_{tr}$  is laminar momentum thickness at  $s = s_{tr}$ .

#### 2.1.4 Ice Accretion: Extended Messinger Model

Extended Messinger model is used to calculate ice accretion. Extended Messinger model is characterized by four equations; conservation of energy equations for ice and water layers, a conservation of mass equation and a phase change or Stefan condition at the ice/water interface [30].

$$\frac{\partial T}{\partial t} = \frac{k_i}{\rho_i C p_i} \frac{\partial^2 T}{\partial y^2} \quad (2.19)$$

$$\frac{\partial \theta}{\partial t} = \frac{k_w}{\rho_w C p_w} \frac{\partial^2 \theta}{\partial y^2} \quad (2.20)$$

$$\rho_i \frac{\partial B}{\partial t} + \rho_w \frac{\partial h}{\partial t} = \rho_a \beta V_\infty + \dot{m}_{in} - \dot{m}_{e,s} \quad (2.21)$$

$$\rho_i L_F \frac{\partial B}{\partial t} = k_i \frac{\partial T}{\partial y} - k_w \frac{\partial \theta}{\partial y} \quad (2.22)$$

where  $\theta$  and  $T$  are the temperatures,  $k_i$  and  $k_w$  are thermal conductivities,  $C p_i$  and  $C p_w$  are the specific heats and  $h$  and  $B$  are the thickness of water and ice layers, respectively. In equation 2.21,  $\rho_a \beta V_\infty$ ,  $\dot{m}_{e,s}$ ,  $\dot{m}_{in}$  are impinging, evaporating/sublimating and runback water mass flow rates for a panel, respectively. Meanwhile,  $\rho_i$  and  $L_F$  refer to the density of ice and the latent heat of solidification of water. First, boundary and initial conditions must be identified to find out the ice and water thicknesses together with the temperature distribution at each layer. These are based on the following assumptions :

- Ice is in perfect contact with the surface of the aerodynamic profile :

$$T(0, t) = T_s \quad (2.23)$$

Surface temperature is taken as the temperature of recovery:

$$T_s = T_a + \frac{V_\infty^2 - U_e^2}{2C_p} \frac{1 + 0.2rM^2}{1 + 0.2M^2} \quad (2.24)$$

In above equation,  $M$  is the flow Mach number and  $r$  is the adiabatic recovery factor.  $M = V_\infty/a_\infty$ , while speed of sound is given by  $a_\infty = \sqrt{\gamma RT_a}$ . The recovery factor is a function of Prandtl number and depends on the flow regime. It is taken as  $r = \sqrt{Pr}$  for laminar flow and  $\sqrt[3]{Pr}$  for turbulent flow.

- The temperature is continuous at the ice/water boundary and is equal to the freezing temperature:

$$T(B, t) = \theta(B, t) = T_f \quad (2.25)$$

- At the air/water (glaze ice) or air/ice (rime ice) interface, flux of heat is identified by radiation ( $Q_r$ ), convection ( $Q_c$ ), cooling by incoming droplets ( $Q_d$ ), aerodynamic heating ( $Q_a$ ), latent heat release ( $Q_l$ ), heat brought in by runback water ( $Q_{in}$ ), evaporation ( $Q_e$ ) or sublimation ( $Q_s$ ) and kinetic energy of incoming droplets ( $Q_k$ ):

$$\text{For glaze ice : } -k_w \frac{\partial \theta}{\partial y} = (Q_c + Q_e + Q_d + Q_r) - (Q_a + Q_k + Q_{in}) \text{ at } y = B + h \quad (2.26)$$

$$\text{For rime ice : } -k_i \frac{\partial T}{\partial y} = (Q_c + Q_s + Q_d + Q_r) - (Q_a + Q_k + Q_{in} + Q_l) \text{ at } y = B \quad (2.27)$$

- Airfoil surface is initially clean:

$$B = h = 0, \quad t=0 \quad (2.28)$$

In this approach, each panel represents a control volume. The above equations are written for each panel and ice is assumed to grow perpendicularly to the panel.

Rime ice formation is defined with a simple algebraic equation from the mass balance in Eqn. 2.21, since impinging water droplets freeze entirely [29]:

$$B(t) = \frac{\rho_a \beta V_\infty + \dot{m}_{in} - \dot{m}_{e,s} t}{\rho_r} \quad (2.29)$$

On the other side, glaze ice thickness is calculated by integrating the ordinary differential equation obtained by combining energy and mass equations over time. The differential equation becomes [30]:

$$\rho_g L_f \frac{\partial B}{\partial t} = \frac{k_i(T_f - T_s)}{B} + k_w \frac{(Q_c + Q_e + Q_d + Q_r) - (Q_a + Q_k + Q_{in})}{k_w + h(Q_c + Q_e + Q_d + Q_r)/(T_s - T_a)} \quad (2.30)$$

In this expression, the detailed information about energy terms and the value of used parameters can be found in study of Özgen and Canibek [30]. Under glaze ice conditions, only a fraction of impinging water freezes. Remaining water may either flow downstream as runback water or may be shed due to high shear. It is assumed that all of the unfrozen water passes to the neighboring downstream cell as runback water at the upper surface, while all water sheds at the lower surface [45]. In order to calculate the glaze ice thickness as a function of time, Eqn. 2.30 is integrated numerically over time for the duration of the exposure time using a Runge-Kutta-Fehlberg method.

### 2.1.5 Multi-layer Calculation Approach and Smoothing Algorithm

Ice formation changes the initial blade profile and this deformation affects the external flow. Therefore in a multi-layer ice accretion process, the total icing exposure time is divided into shorter time segments. At each time segment, the blade profile changes due to ice formation and the external flow field is recomputed. Both the collection efficiency and heat transfer coefficients are then updated. As the ice builds up in the multi-layer approach, this approach is expected to be more accurate due to the fact that the effect of ice accretion on the flow field, droplet trajectories and ice accretion itself is accounted for.

The flow solver used in this study, XFOIL, is prone to exploit model flaws and lead to erroneous conclusions in power loss prediction especially in glaze type ice shapes since the ice thicknesses obtained by solving the 1D conservation equations in the direction normal to the leading edge panels may produce highly oscillatory, jagged ice profiles. For this reason, a new robust smoothing without shrinkage [46] algorithm is implemented into the ice prediction tool. In this algorithm, second order diffusion and anti-diffusion terms are successively applied to the iced geometry as suggested.  $x$  and  $y$  coordinates on the iced surface are smoothed as follows:

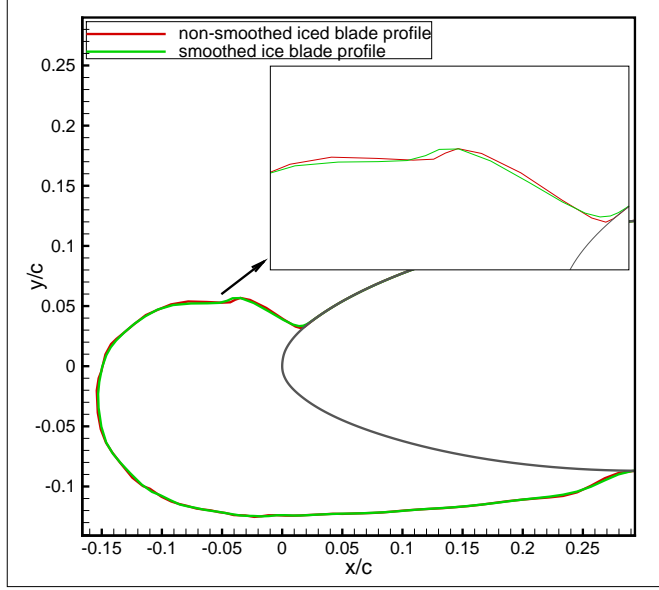


Figure 2.2: Smoothing without shrinkage.

$$\begin{aligned}
 x(n) &= x(n) + \alpha \times (x(n-1) - 2 \times x(n) + x(n+1)), \quad 0 < \alpha < 1 \\
 y(n) &= y(n) + \alpha \times (y(n-1) - 2 \times y(n) + y(n+1))
 \end{aligned}
 \tag{2.31}$$

$$\begin{aligned}
 x(n) &= x(n) - \mu \times (x(n-1) - 2 \times x(n) + x(n+1)), \quad 0 < \mu < 1 \\
 y(n) &= y(n) - \mu \times (y(n-1) - 2 \times y(n) + y(n+1))
 \end{aligned}
 \tag{2.32}$$

where  $\alpha$  represents the diffusion scale factor and  $\mu$  represents the anti-diffusion scale factor. These scale factors can be chosen arbitrary with the condition that the anti-diffusion scale factor should be greater than the diffusion scale factor to perform smoothing without shrinkage in the ice mass as illustrated in Figure 2.2.

### 2.1.6 Error Analysis for Predicted Ice Shapes

To determine the accuracy of the predicted ice shapes acquired with the computational tool, validation studies are carried out in which the present study results are matched against the available experimental and numerical data. For this aim, a methodology introduced by Ogretim et al. [12] is used for error analysis instead of the RMS values. In this new methodology, the calculated error in neighborhoods of slight ice thickness

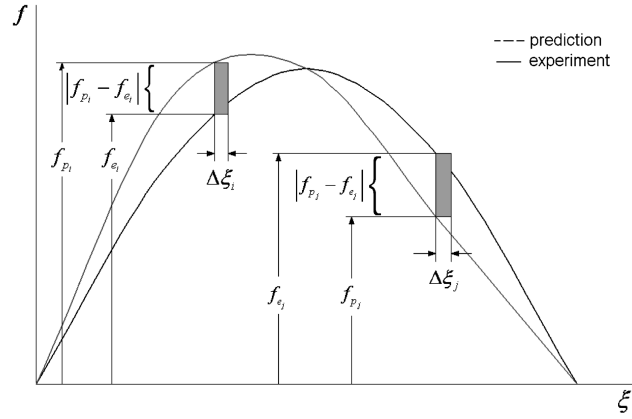


Figure 2.3: Geometrical illustration for the cumulative error [12].

does not add as much to the overall error as the neighborhoods of large ice thickness. In this method, instead of the ice cross-sectional area error, a dedicated error evaluation was developed. Here, the absolute value of the local relative difference between the prediction and the experiment is used. This weighted relative error is calculated by the following relation:

$$\epsilon = \frac{\sum_{n=1}^N |f_{ei} - f_{pi}| \Delta \xi_i}{\sum_{n=1}^N |f_{ei}| \Delta \xi_i} \quad (2.33)$$

where subscript  $p$  refers the estimated ice thickness, subscript  $e$  shows the experimental ice thickness and  $N$  represents the total number of data points. The ratio of the area between prediction and the experiment to the experimental ice area is equivalent to area weighted true relative error. In this error computation, iced region is not compared but the amount of accreted mass on the surface is take in consideration since the ice shape area would not indicate how exactly the predicted ice shape matched with the experimental one. In Figure 2.3, two different shapes which have the same area is depicted.

## 2.2 Blade Element Momentum Theory

The BEM methodology is used widely in wind turbine design and performance analysis due to its accuracy and ease of implementation. Blade is divided into finite elements along the span and 2D solutions in each section is used to reconstruct the

3D flow field and the loading on the blade. The BEM module provide the value of sectional velocities and angles of attack to predict ice shape for each blade element of the turbine. In order to obtain more accurate sectional aerodynamic loads in the BEM formulation (especially the drag coefficient), flow over clean and iced blade profiles are solved by XFOIL [43]. It is an open source software used for the design and analysis of subsonic airfoils. XFOIL implements a linear-vorticity second order accurate panel method, and is coupled with an integral boundary-layer method and an  $e^n - type$  transition prediction formulation.

Blade Element Momentum Theory combines two methods for analyzing the performance of the horizontal axis wind turbine. In the first method, momentum balance on a rotating annular stream tube passing through a turbine is used. Secondly, the forces generated by the airfoil lift and drag coefficients at various sections along the blade are investigated. These two methods then yield a sequence of equations that can be solved iteratively.

### 2.2.1 Blade Element Theory

Blade Element Theory depends on three important assumptions:

- Spanwise velocity components along the blade are neglected.
- Aerodynamic interactions between different blade sections are ignored.
- The forces on the blade sections are only determined by the lift and drag coefficients.

Consider a turbine blade split up into  $N$  elements as illustrated in Figure 2.4. Each of the blade sections confronts a slightly different flow velocity and an angle of attack as they have a different chord length ( $c$ ), and experience a different rotational speed ( $\Omega r$ ) and a different twist angle ( $\gamma$ ). Thus, each section experiences specific lift and drag force which are found by relations:

$$dL = \frac{1}{2} \rho U_t^2 C_l c dr \quad (2.34)$$

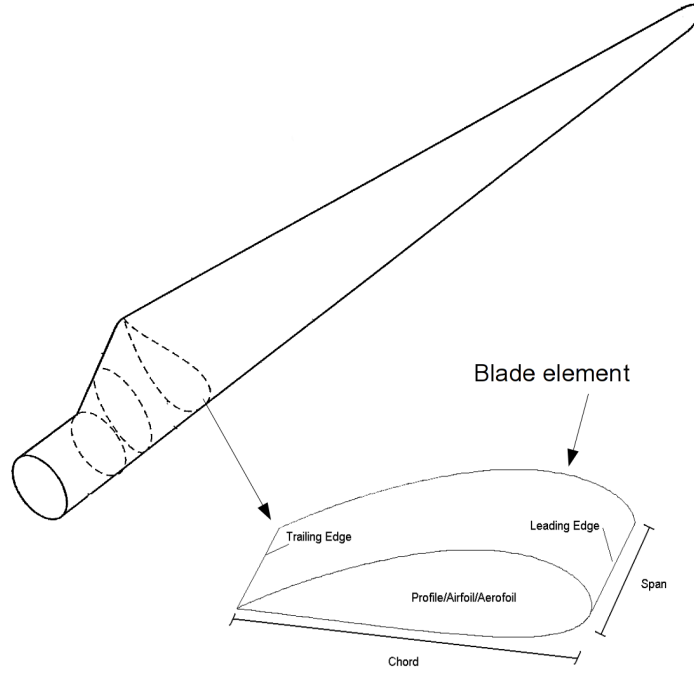


Figure 2.4: The Blade Element Model.

$$dD = \frac{1}{2} \rho U_t^2 C_d c dr \quad (2.35)$$

The BEM theory necessitates dividing up the turbine blade into an adequate number (approximately up to 20) of sections and computing the flow at each blade element. Total power and thrust are estimated by cumulative sum of the blade sections.

### 2.2.2 Method Used in This Study

The performance analysis with BEM theory is the estimation of sectional velocities, sectional angles of attack and thrusts for each blade section individually. In order to perform the analysis induction factors are required to be computed in an iterative process.

In order to decrease the number of the steps for iterative induction factors prediction, initial values for induction factors are taken as zero, initially. Then, next stage is to compute the inflow angle by using axial induction factors predicted:

$$U_t = \sqrt{U_\infty^2 (1 - a)^2 + \Omega^2 r^2 (1 + a')^2} \quad (2.36)$$

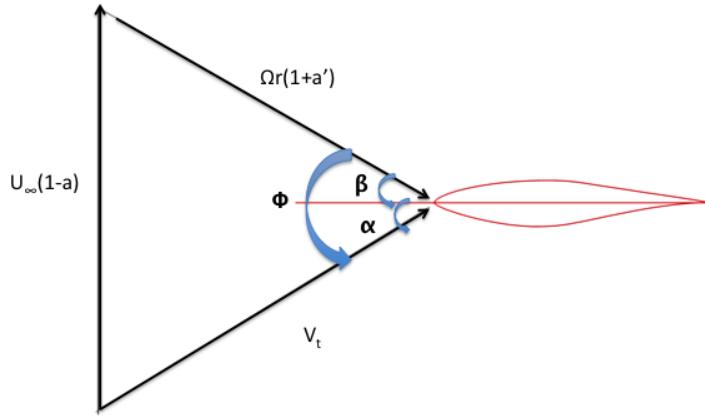


Figure 2.5: Velocity triangle for a blade element.

From Figure 2.5, it can be seen that sectional velocity at each blade element is related to the induction factors as given in Equation 2.37.

$$\tan \phi = \frac{U_\infty(1-a)}{\Omega r(1+a')} \quad (2.37)$$

The value of  $\beta$  comes from planform data of the wind turbine, so angle of attack is calculated from

$$\alpha = \phi - \beta \quad (2.38)$$

The next phase is to evaluate the tip loss factor and thrust coefficient. Solidity is defined as the fraction of the annular area that is covered by blades and expressed as follow;

$$\sigma' = \frac{Bc}{2\pi r} \quad (2.39)$$

Tangential and axial induction factors are expressed as;

$$a' = \left( \frac{4 \sin \phi \cos \phi}{\sigma'(C_l \sin \phi - C_d \cos \phi)} - 1 \right)^{-1} \quad (2.40)$$

$$a = \left( \frac{4 \sin^2 \phi}{\sigma'(C_l \cos \phi + C_d \sin \phi)} + 1 \right)^{-1} \quad (2.41)$$

$$C_T = \frac{\sigma'(1-a)^2(C_l \cos \phi + C_d \sin \phi)}{\sin^2 \phi} \quad (2.42)$$

$$F = \frac{2}{\pi} \cos^{-1} \left( \exp \left( - \frac{B R - r}{2 r \sin \phi} \right) \right) \quad (2.43)$$

As soon as the tip loss factor and thrust coefficient are computed, the axial induction factor is attained. If  $C_T > 0.96F$ , then the blade is accepted as highly loaded and modified Glauert correction is applied:

$$a = \frac{18F - 20 - 3\sqrt{C_T(50 - 36F) + 12F(3F - 4)}}{30F - 50} \quad (2.44)$$

If the turbine blade is lightly loaded, the standard Blade Element Momentum theory is used:

$$a = \left( \frac{4F \sin^2 \phi}{\sigma'(C_l \cos \phi + C_d \sin \phi)} + 1 \right)^{-1} \quad (2.45)$$

$$a' = \left( \frac{4F \sin \phi \cos \phi}{\sigma'(C_l \sin \phi - C_d \cos \phi)} - 1 \right)^{-1} \quad (2.46)$$

After obtaining the induction factors, thrust and torque of each blade element can be computed from the equations below.

$$dT = B \frac{1}{2} \rho V_t^2 (C_l \cos \phi + C_d \sin \phi) c dr \quad (2.47)$$

$$dQ = B \frac{1}{2} \rho V_t^2 (C_l \sin \phi + C_d \cos \phi) c r dr \quad (2.48)$$

The power produced by the wind turbine is then calculated from the total torque value:

$$P = \Omega Q \quad (2.49)$$

Throughout the iteration process, lift and drag coefficients are calculated by using XFOIL. For each blade element, the sectional blade profile together with the planform data ie. twist angle, chord length are required.

### **2.2.3 Algorithm of the BEM Theory**

Axial and tangential induction factors are computed iteratively. The tolerance for convergence is taken as  $10^{-4}$  in the light of the results of the sensitivity analysis for this study. The convergence must be achieved for both axial and tangential induction factors to proceed with the power evaluation. The algorithm steps of this procedure are depicted in Figure 2.6.

## **2.3 Coupling BEM Theory with Ice Accretion Prediction Tool**

Combining the BEM theory with ice accretion prediction tool is based on the input-output style file creation to pass information between program modules. Initially, power production of the clean turbine blade is calculated by using BEM Theory tool developed. Next, the ice accretion prediction methodology developed is employed to predict the two dimensional ice profiles on the blade sections along the span. The sectional inflow velocities and the angles of attack are provided by the BEM solution for the clean blade. Section ice accretions are then computed based on the local flow properties and the given atmospheric icing conditions. Once the sectional ice profiles are computed, the BEM tool is again employed to compute the power production of the iced turbine. Unlike the power production of the clean blade case, full turbulence condition is imposed by applying forced transition at the leading edge of the iced blade profiles during XFOIL computations.

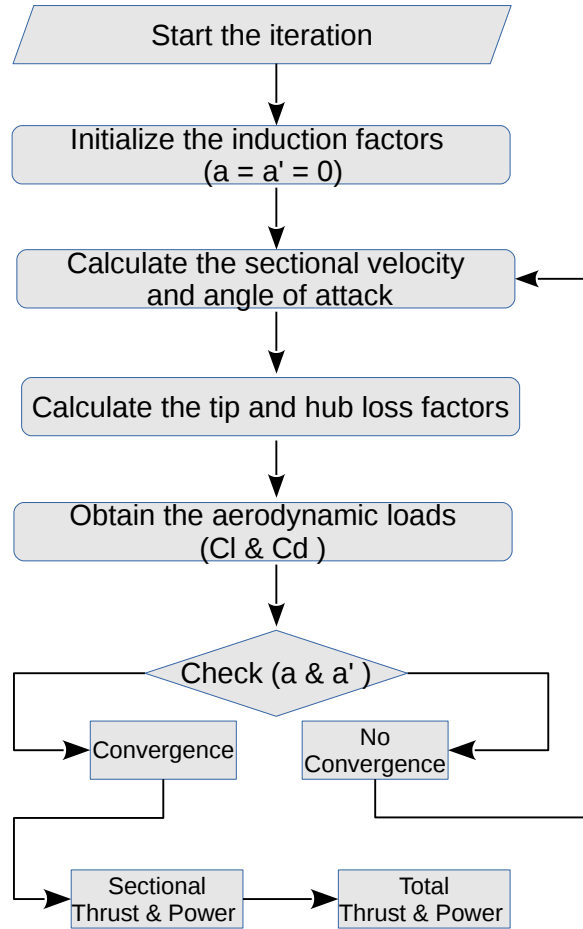


Figure 2.6: Flowchart of the algorithm of BEM Theory.

## 2.4 Gradient Based Aerodynamic Shape Optimization

One of the most critical issues facing the optimization of wind power production in cold climates is ice accretion on turbine blades. It is important to minimize ice accumulation and induced power production losses while keeping clean turbine's power production same in the aerodynamic shape optimization process. For this aim a gradient-based optimization technique coupled with simple line search algorithm is employed in the shape optimization process. The objective function,  $O$ , is taken as the power production of the iced blade based on BEM methodology. The optimization algorithm acts as a driver for all the modules. It first calls the ice accretion module, which provides the iced blade profiles at the spanwise blade sections. The

BEM module then computes the power production of the iced turbine. In the optimization process, the blade geometry is deformed by applying Hicks-Henne bump functions over the leading edge of the airfoil. For the first time, these bump functions were identified by Hicks et al. [47] in 1977, and used in wing design optimization by Hick and Henne [48]. The shape functions are defined as:

$$f_i(x) = \sin^{t_i}(\pi x^{m_i}), \quad m_i = \frac{\ln(0.5)}{\ln(h_i)}, \quad i = 1, \dots, n.$$

where  $n$  stands for the number of basis functions,  $h_i$  is the location of the maxima and  $t_i$  controls the width of the functions. In this study, there are three Hicks-Henne shape functions both for the upper and lower surfaces, respectively ( $n=6$ ). The perturbations are added on the baseline to modify the initial blade profile.

$$y = y_0 + \sum_{i=1}^n f_i(x)$$

Figure 2.7 shows this set of three Hicks-Henne sine bump functions which is applied to the baseline blade profile. These Hicks and Henne bump functions are adapted such that only specific regions are disturbed, while the rest of airfoil coordinates remain unchanged. A simple line search algorithm is also employed to maximize the objective function along the gradient vector.

- Blade profile around the leading edge is modified by bump functions.
- Amplitudes of the bump functions,  $A_i$  become design variables.
- Gradient of the objective function with respect to design variables are evaluated by finite differences:

$$\frac{\partial O}{\partial A_i} \approx \frac{O(A_i + \epsilon) - O(A_i)}{\epsilon}$$

Optimum design variables are searched along each gradient vector along the optimization steps. The flowchart of the developed computational tool is presented in Figure 2.8.

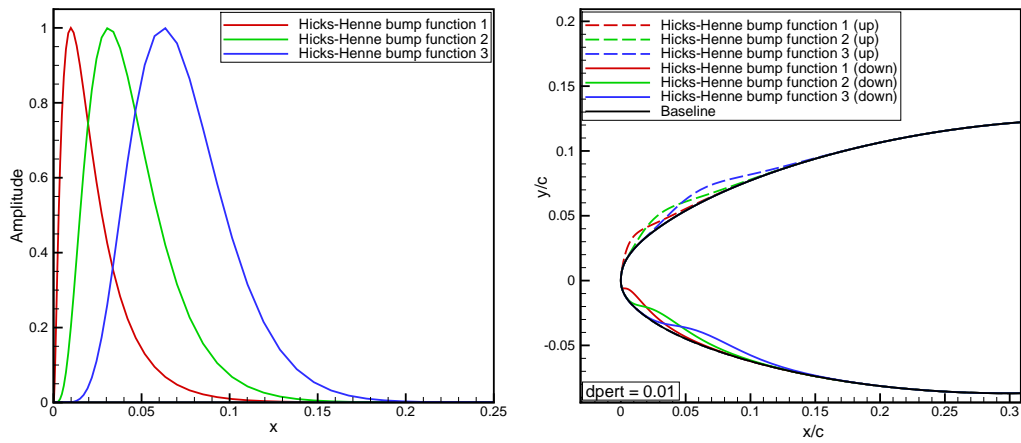


Figure 2.7: Hicks-Henne bump functions (top) and its effect on a baseline airfoil (bottom).

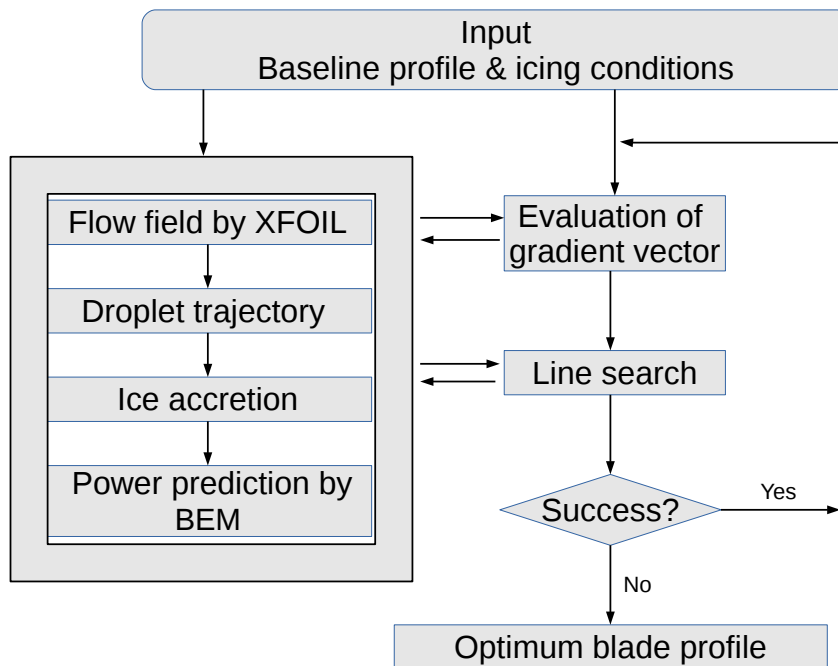


Figure 2.8: Flowchart of Methodology.



## CHAPTER 3

### RESULTS AND DISCUSSION

In this section, the tools developed for ice accretion on wind turbine blades and wind power production predictions are first validated against the experimental data and other numerical solutions. Rime and glime ice conditions are mostly considered. Flow fields and aerodynamic load predictions of XFOIL for clean and iced DU93-W-210 blade profiles are also compared against the predictions of the Navier-Stokes solver, SU2. Power production losses under various icing conditions and wind speeds are then investigated for the Aeolos-H 30kW and NREL 5MW wind turbines. Finally, a shape optimization study is performed for the Aeolos-H 30kW wind turbine blades for minimizing the ice accretion at the rated wind speed.

#### 3.1 Validation Cases for Ice Accretion Prediction

The ice accretion methodology developed is first validated against the experimental and computational study performed by Han et al. [13] at Adverse Environment Rotor Test Stand (AERTS). AERTS is designed to generate an accurate icing cloud around a test rotor to validate the capability of the facility to reproduce representative icing conditions for numerical simulations. Information about the AERTS experimental set-up and the performed icing events are given in detail in Reference [13]. In the experiments, an S809 turbine blade profile with a chord length of  $0.267m$  is used to observe the rime and glaze ice formations while keeping the liquid water content less than  $1.5 g/m^3$ . In addition, the LEWICE predictions are obtained for the rime ice cases [13]. LEWICE [49] is an ice accretion prediction tool developed by NASA. The icing conditions used in the validation cases are given in Table 3.1. In the numerical

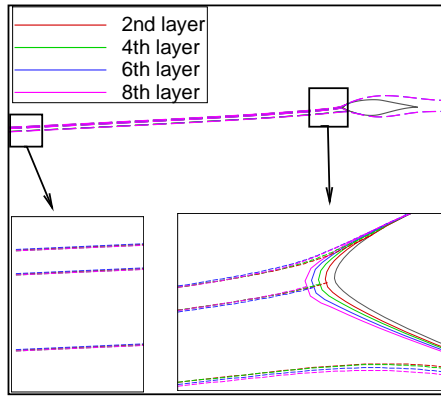
simulations, the total icing exposure time is  $30min$ , and a multi-layer approach is implemented. The results obtained are given in Figures 3.1–3.3.

Table 3.1: Atmospheric icing conditions (Blade profile=S809, Chord=0.267 m, Ambient pressure=95610 Pa, Humidity=100%).

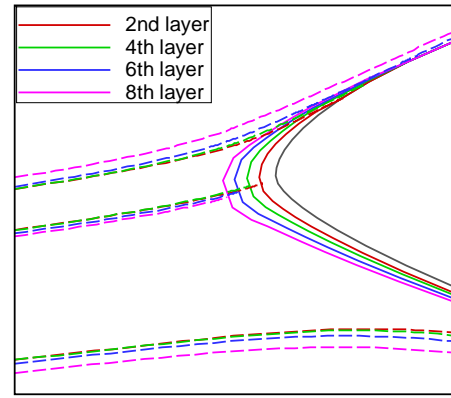
Case	Ref.	Ice	$V_\infty$	$\alpha$	LWC	MVD	$T_a$	$t_{exp}$
	Case [13]	type	(m/s)	(degree)	(g/m <sup>3</sup> )	( $\mu m$ )	( $^\circ C$ )	(min)
1	16	rime	50	2 $^\circ$	0.08	20	-4.5	30.0
2	17	rime	50	4 $^\circ$	0.08	20	-7.0	30.0
3	24	glaze	43	6 $^\circ$	0.3	20	-9.0	12.0

In Figure 3.1, the droplet trajectories, collection efficiency distributions, formation of multi-layer ice shapes and the comparison of the final ice profile with the experimental data are presented for Case 1. In multi-step computations, the impingement zones and the maximum collection efficiencies vary with each time step as depicted in Figure 3.1-b,c. The collection efficiency distribution, in general, has a maximum in the vicinity of the leading edge and quickly diminishes in the downstream direction on both the upper and the lower surfaces of the blade profile. But, the variations in multi-layer computations are expected since the droplet trajectories depend on the velocity field, and the velocity field is updated at each step as the ice layers are added (Figure 3.1-d). As shown in Figure 3.1-e, as opposed to the single step solution the multi-step solutions converge to the same rime ice profile, and they are in good agreement with the experimental data and the LEWICE predictions.

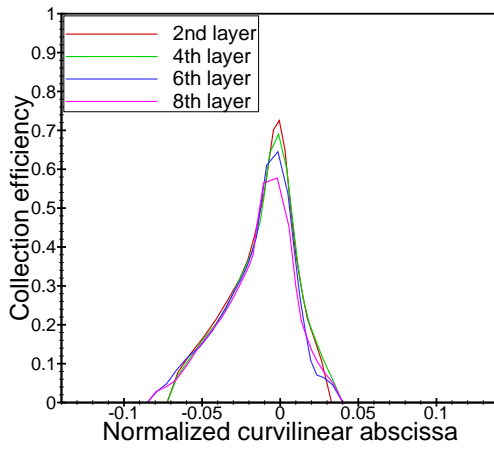
The variation of collection efficiencies and the ice profiles along the multi-step computations are similarly given for Case 2 and 3 in Figure 3.2 and Figure 3.3. In Case 3, where the LWC is higher, a glaze ice formation is observed and the converged solution is only obtained for 8 and 10 step computations. In both cases, ice is mainly collected over the pressure side of the blade, which is attributed to the higher angle of attack of the blades. Although the ice formation on the upper surface is underpredicted, the maximum ice thicknesses predicted agree well with the experimental data for both cases (Figure 3.2-b and Figure 3.3-b). It should be noted that the glaze ice formation is usually more difficult to predict, which is attributed to the low fidelity of



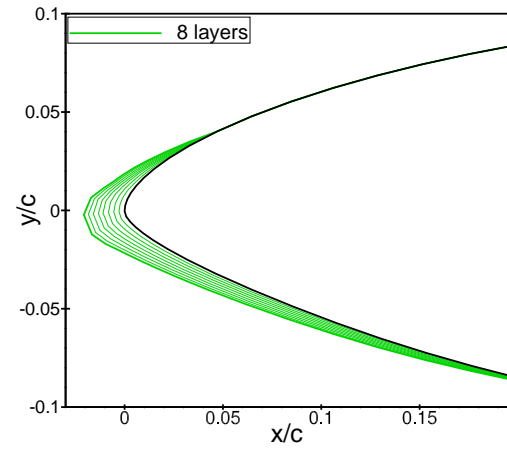
(a) Particle droplet trajectories with 8-layer computation



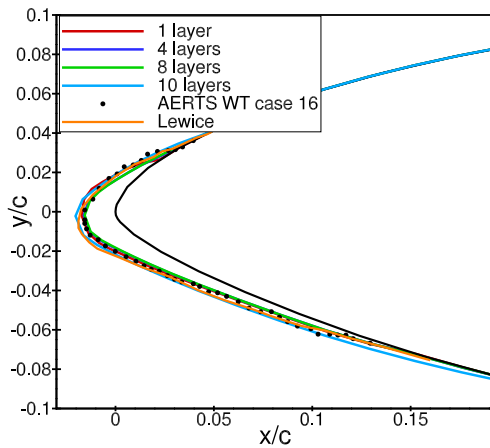
(b) Particle droplet trajectories with 8-layer computation



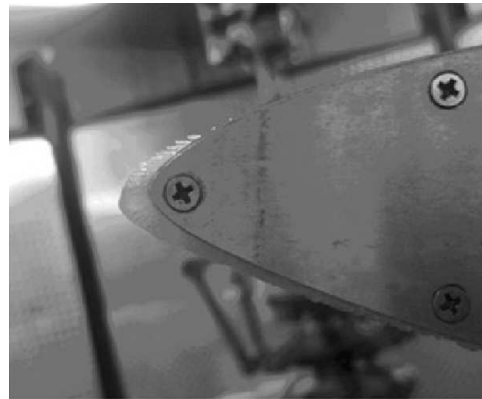
(c) Collection efficiencies with 8-layer computation



(d) Growth of ice shape with 8-layer computation

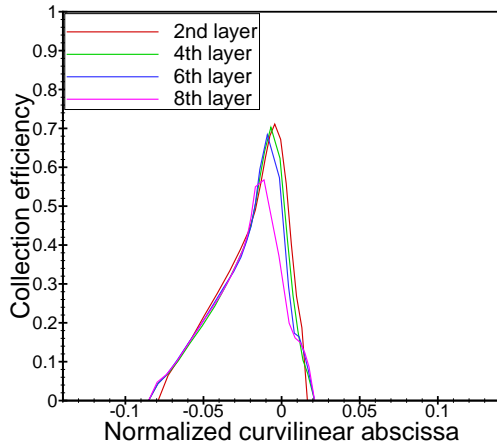


(e) Predicted and measured ice profiles

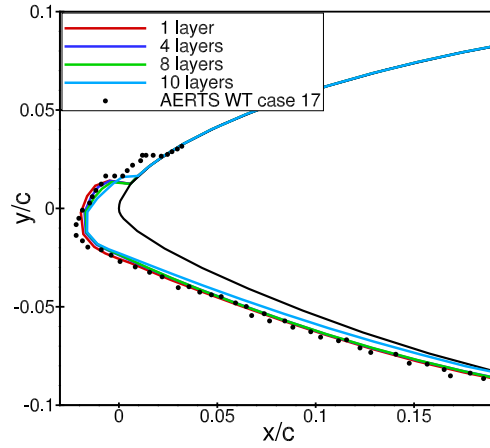


(f) Iced blade for AERTS case 16 [13]

Figure 3.1: Predicted ice shapes for S809 blade profile for conditions in Table 3.1 for AERTS case 16 [13].

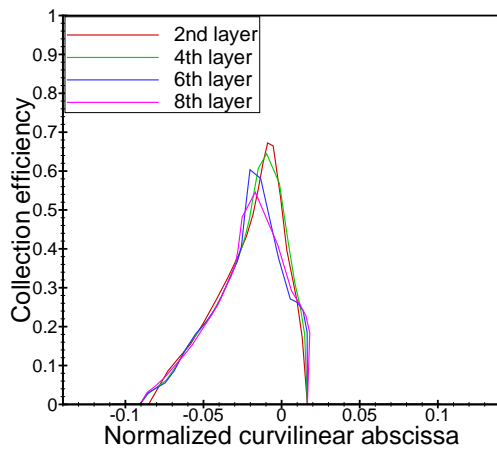


(a) Collection efficiencies with 8-layer computation

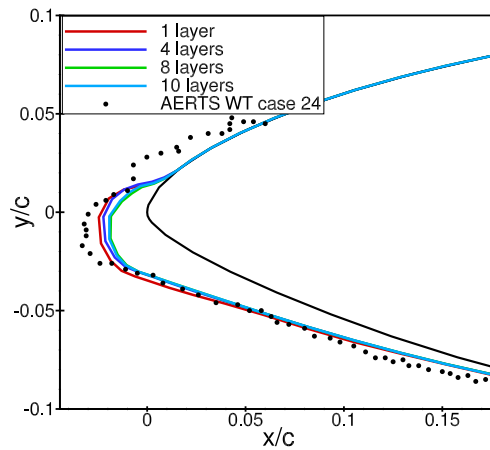


(b) Predicted and measured ice profiles

Figure 3.2: Predicted ice shapes for S809 blade profile for conditions in Table 3.1 for AERTS case 17 [13].



(a) Collection efficiencies with 8-layer computation



(b) Predicted and measured ice profiles

Figure 3.3: Predicted ice shapes for S809 blade profile for conditions in Table 3.1 for AERTS case 24 [13].

the runback water model.

The error in the prediction of ice profiles is also assessed by comparing the ice volumes against the measured data (Table 3.2). In Case 1 the error in the ice volume predicted by the present study is less than that of LEWICE, and both are less than 5%. Since the multi-step computations for all 3 cases show a convergence in 8 steps and higher, 8 step solutions are used for the rest of the ice accretion predictions.

Table 3.2: Percent error in predicted ice volume for S809 blade profile.

Cases	1 layer	4 layers	8 layers	10 layers	LEWICE
case 1	8.6	2.4	2.4	2.4	4.8
case 2	9.2	12.9	13.5	13.5	–
case 3	19.8	22.4	25.5	25.6	–

In the second group of validation cases, DU 93-W-210 blade profile, which is commonly used in pitch controlled wind turbines, is considered in the full scale and in a testing scale. The icing and flow conditions in the reference experimental study of Blasco et al. [50] are presented in Table 3.3. It should be noted that the exposure times in the scaled study is adjusted [50] for similarity. All simulations are performed in a multi-step computation by using 8 steps.

Table 3.3: Atmospheric icing conditions.

Case	Ref.	Ice	LWC	MVD	$T_a$	$t_{exp}$
	Case [50]	type	( $g/m^3$ )	( $\mu m$ )	( $^{\circ}C$ )	(min)
Full scale (Chord=1.45 m, Free-stream velocity=50 m/s, $\alpha=0^{\circ}$ )						
4	3	Freezing fog	0.22	30	-9.7	45.0
5	5	Freezing fog	0.10	28	-21.3	45.0
6	6	Freezing drizzle	0.26	250	-8.1	45.0
Testing scale (Chord=0.725 m, Free-stream velocity=41 m/s, $\alpha=0^{\circ}$ )						
7	3	Freezing fog	0.26	17	-9.9	14.0
8	5	Freezing fog	0.12	16	-21.5	13.7
9	6	Freezing drizzle	0.3	143	-8.3	14.2

The predicted ice profiles for all the cases are given in Figure 3.4, and are compared with the reference study [50] and the available LEWICE prediction for Case 4 only. It should be noted that in all these cases the liquid water content is high and the runback water is present, which causes mixed and glaze ice formations. The reference Case 6 has the largest droplet size. Large droplets follow more ballistic trajectories resulting in a wider impingement zone and higher collection efficiencies, which result in larger ice accumulation. Although the ice volumes in all the cases are underpredicted, the

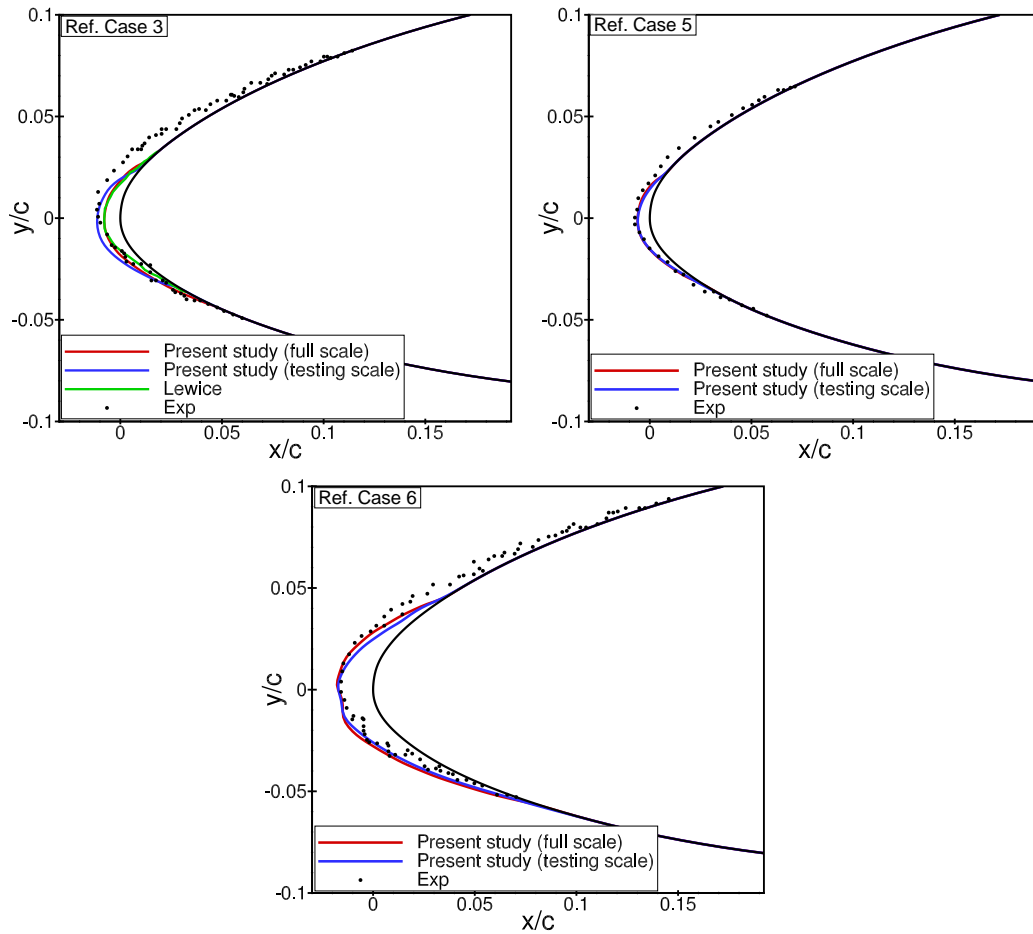
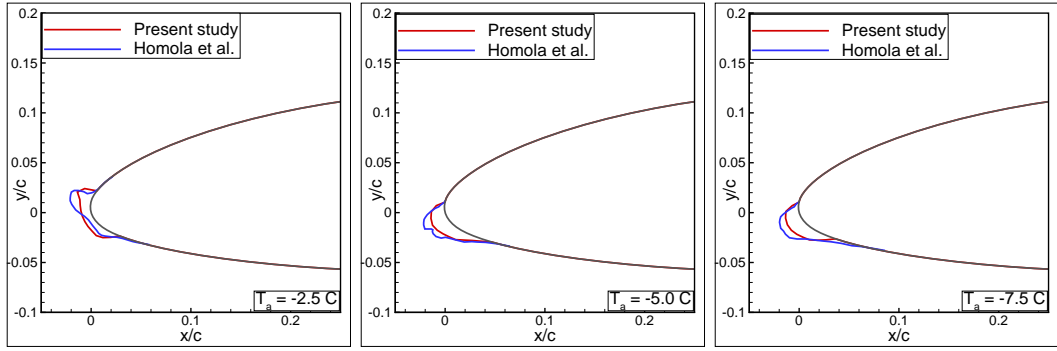


Figure 3.4: Predicted ice shapes for DU 93-W-210 for conditions given in Table 3.3.

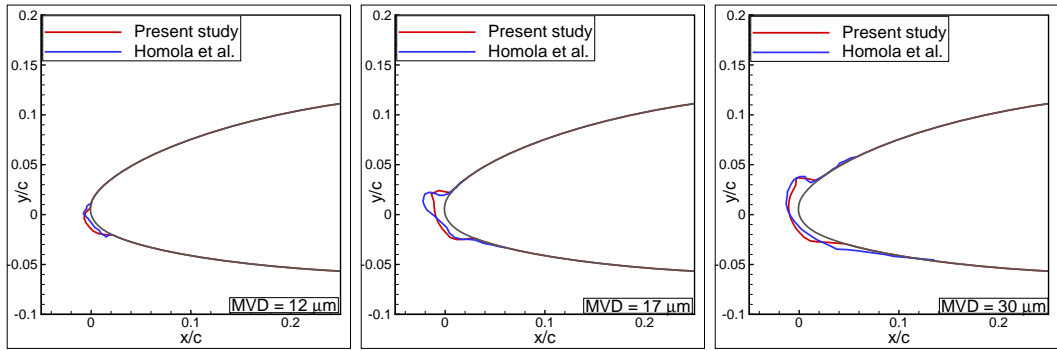
ice profiles and the ice thicknesses predicted are, in general, in good agreement with the experimental data and with the LEWICE prediction. The error in ice volumes predicted is similarly assessed in Table 3.4. The underprediction of the ice formations on the upper surface is similarly attributed to the low fidelity of the runback water model.

### 3.1.1 Effect of Droplet Size and Temperature on Icing

In this validation case, a 5MW pitch controlled wind turbine blade profile (NACA 64618) and NACA 0012 airfoil are used to investigate the effects of the atmospheric temperature and droplet size on the ice accretion. The geometric and flow conditions in the reference studies are presented in Table 3.5.



$d_p = 17 \mu\text{m}$



$T_a = -2.5 \text{ }^\circ\text{C}$

Figure 3.5: Predicted ice profiles for NACA 64618 airfoil for conditions in Table 3.5

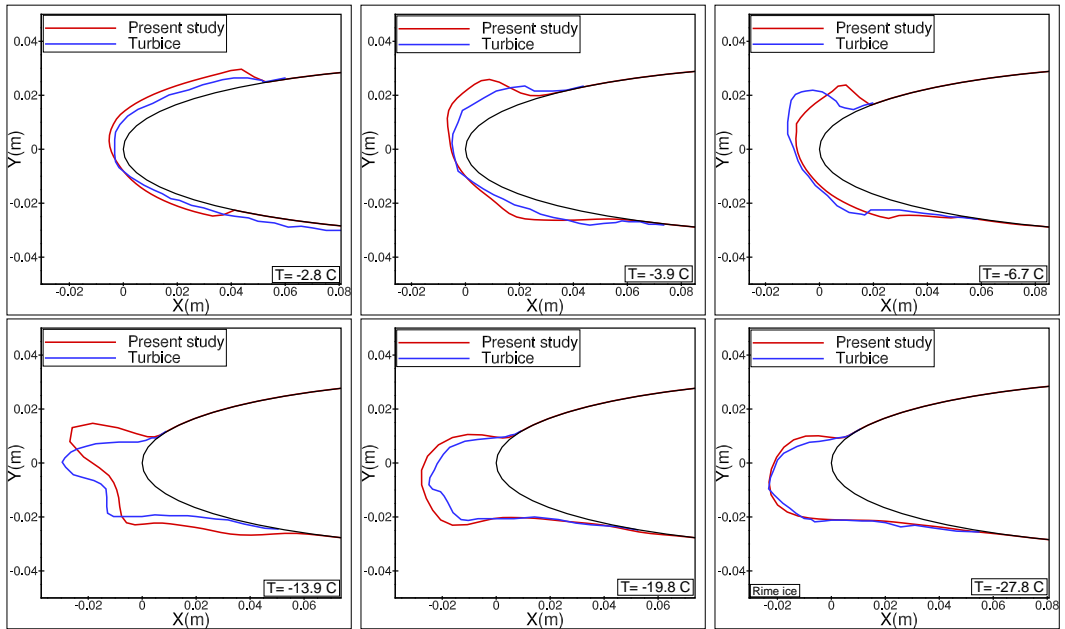


Figure 3.6: Predicted ice profiles for NACA 0012 airfoil for conditions in Table 3.5.

Table 3.4: Percent error in predicted ice volume for DU 93-W-210 blade profile.

Cases	Present study (full scale) % error	Present study (testing scale) % error	LEWICE % error
Ref. Case 3	20.5	23.2	26.1
Ref. Case 5	14.5	15.0	–
Ref. Case 6	6.2	7.4	–

Table 3.5: Geometric characteristics and flow conditions used in the calculations.

Airfoils	NACA 64618	NACA 0012
Chord	1.9 m	0.53 m
Angle of attack	5 °	4 °
Relative air speed	25.7 m/s	58.1 m/s
Liquid water content	0.2 g/m <sup>3</sup>	1.3 g/m <sup>3</sup>
Droplet diameter	12, 17, 30 μ m	20 μ m
Ambient temperature	-2.5, -5, -7.5 °C	-2.8, -3.9, -6.7, -13.9, -19.8, -27.8 °C
Exposure time	120 minutes	8 minutes
Ambient pressure	101300 Pa	101300 Pa
Humidity	100 %	100 %

The results obtained are compared against the numerical study of Homola et al. [51]. In Figure 3.5 the computed ice shapes are in fair agreement with those obtained numerically by Homolo et al. (Turbice). Obtained results in Figure 3.5 suggest that the ice shapes for  $T_a = -5$  °C and  $-7.5$  °C are quite similar and exhibit rime ice characteristics. On the other hand, the ice shape obtained for  $T_a = -2.5$  °C is typically of glaze type and is significantly different from the other two since it has a horn on the upper surface just downstream of the leading edge. These results are expected because rime ice typically occurs at low temperatures and low liquid water contents, as in the first case where  $T_a = -5$  °C and  $-7.5$  °C. However,  $T_a = -2.5$  °C is a significantly high temperature in terms of ice formation and hence yields a glaze ice formation. Results in Figure 3.5 demonstrate that as the droplet size increases, both the ice mass and the extent of the iced region grow. Large droplets yield higher collection efficiencies by

following more ballistic trajectories as explained above. Such a condition generates a wider and a larger ice accretion as seen in Figure 3.5.

In the last validation case, The present method developed is applied to a series of icing events on a NACA0012 airfoil, which are studied numerically by Makkonen et al. [52] using a similar methodology named TURBICE. The ice shapes predicted are compared with the reference study in Figure 3.6. It should be noted that since the liquid water content is relatively high, at ambient temperature values down to  $-13.9^{\circ}C$  glaze ice is formed, whereas at lower temperatures rime ice is formed. It is observed that both the glaze and the rime ice predictions are in reasonably good agreement. Atmospheric pressure, runback water, humidity, break up, splash effects are the information which are missing may cause any discrepancy observed.

### **3.2 Validation of Power Production Predictions**

The BEM tool developed is used to predict the aerodynamic performance of a wind turbine in terms of the generated power both for clean and iced blades. The BEM tool also provides the sectional velocities and the angle of attacks as input to the ice accretion prediction tool. The BEM tool is validated against the experimental data for various wind turbines. First, the verification of the potential flow solver, XFOIL, is carried out for iced blade profiles.

#### **3.2.1 Verification of XFOIL Predictions for an Iced Blade Profile**

The BEM methodology used in the power production estimation requires sectional aerodynamic loads along the blade, which are obtained by using the panel code XFOIL for both clean and iced blades. In this section the flow fields and the aerodynamic loads for an iced DU93-W-210 blade profile, given in Figure 3.7, are evaluated by both XFOIL and an open-source Navier-Stokes solver, SU2 [53], and are compared for verification. SU2 is an open-source collection of CFD tools initially developed at Stanford University. It is written in C++ and Python; is capable of solving a range of flow problems [54]. In the current study, the compressible RANS equations with the  $k-\omega$  SST turbulence model and the ROE fluxes (version 6.1) are employed.

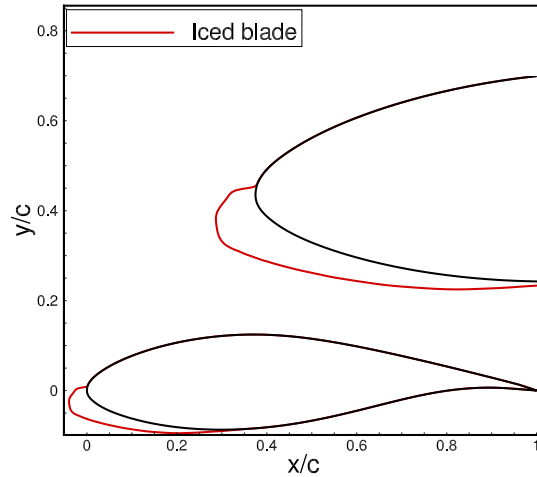


Figure 3.7: Clean and iced DU93-W210 blade profiles.

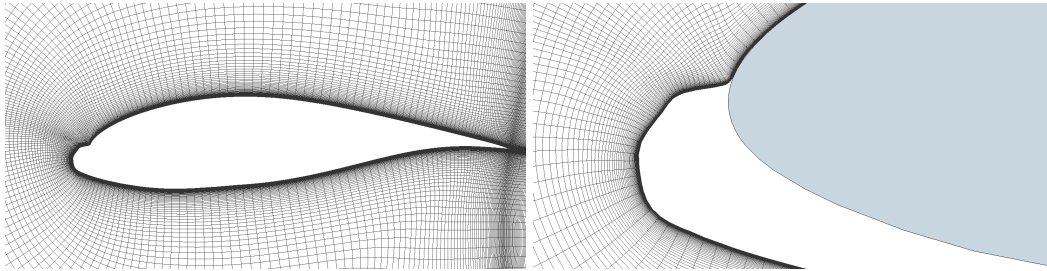
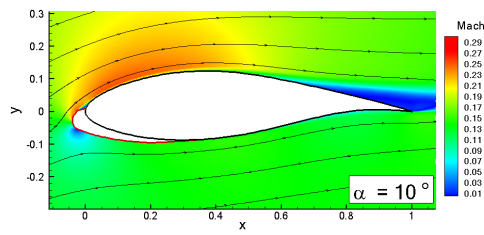


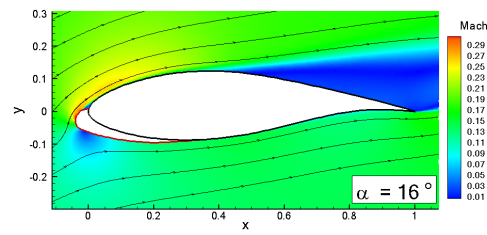
Figure 3.8: Computational mesh used for generating iced airfoil polars with 100k cells on a structured grid topology.

The computational grid for an iced blade profile is given in Figure 3.8. The flow field for high angles of attack of 10 and 16 deg computed by SU2 are given in Figure 3.9. As shown in Figures 3.9-a-d, the SU2 solutions predict recirculating flow regions in the cavity formed by ice accretion, and large trailing edge separation zones. The surface streamlines predicted by the XFOIL solution (Figure 3.9-e-f) similarly reveal recirculating regions and large flow separation zones. The surface pressure distributions predicted are also compared in Figures 3.9-g-h. It is noted that XFOIL slightly under-predicts the suction pressure at these high angle of attacks. Nevertheless, the flow field and the aerodynamic load predictions by XFOIL are, in general, in good agreement with the SU2 predictions.

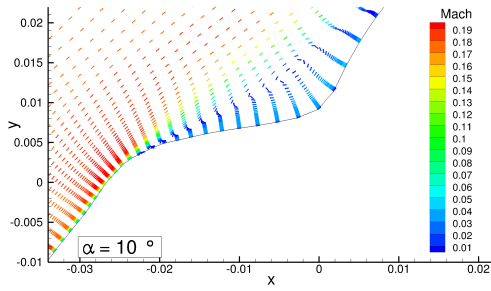
The variations of aerodynamic loads with respect to angle of attack are given in Fig-



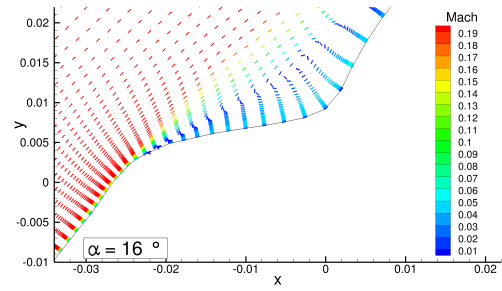
(a) Streamlines predicted by SU2



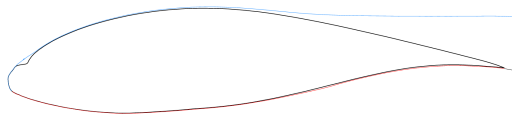
(b) Streamlines predicted by SU2



(c) Recirculation region predicted by SU2



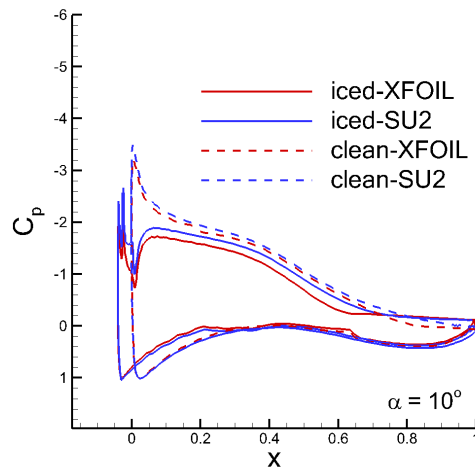
(d) Recirculation region predicted by SU2



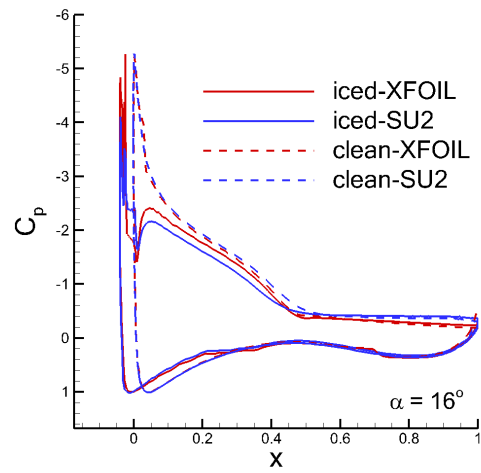
(e) Surface streamline predicted by XFOIL



(f) Surface streamline predicted by XFOIL



(g) Surface pressure distribution ( $\alpha = 10^\circ$ )



(h) Surface pressure distribution ( $\alpha = 16^\circ$ )

Figure 3.9: Flow fields and surface pressure distributions predicted by SU2 and XFOIL.

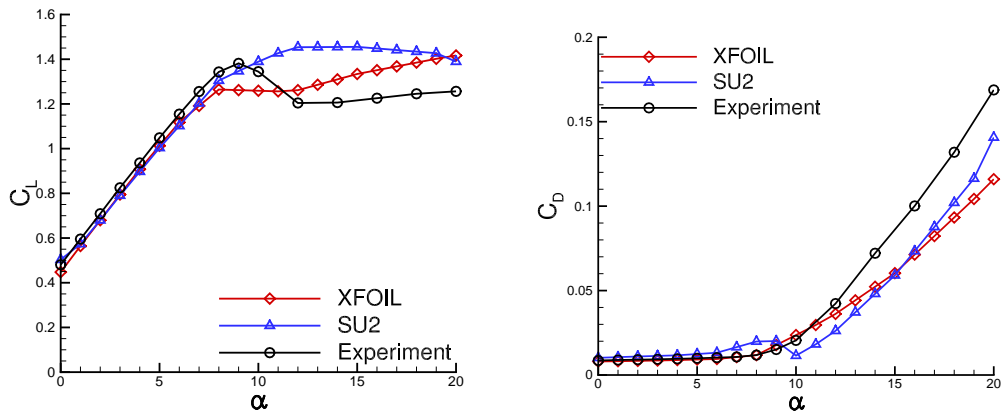


Figure 3.10: Aerodynamic coefficients of clean DU93-W-210 blade profile at  $Re = 1.0 \times 10^6$ .

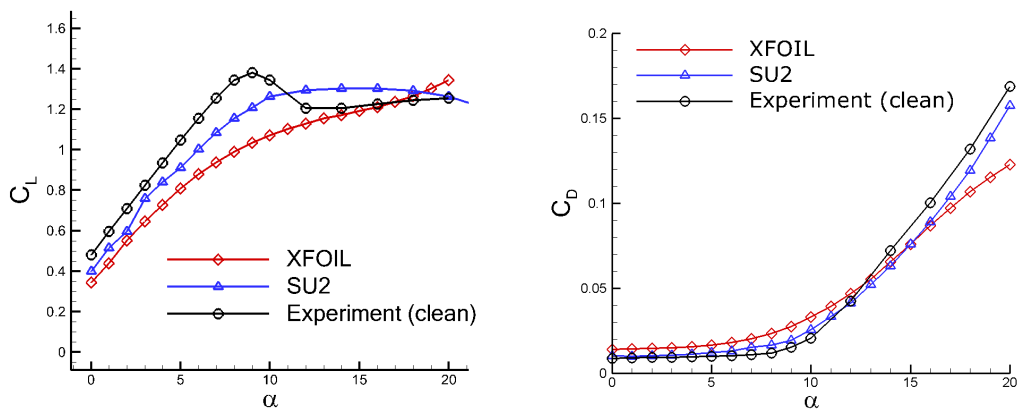


Figure 3.11: Aerodynamic coefficients of iced DU93-W-210 blade profile at  $Re = 1.0 \times 10^6$ .

ures 3.10 and 3.11 for both clean and iced blade profiles. It is observed the XFOIL and SU2 predictions for clean blade profile are in good agreement with the experimental data. Although XFOIL under predicts the lift at high angles of attack for the iced profile, it provides satisfactory results for low angles of attack in the attached flow regime for both iced and clean blade profiles. It is concluded that being efficient and sufficiently accurate, XFOIL may effectively be used in ice accretion predictions and shape optimization studies.

### 3.2.2 Validation of the BEM Tool

Performance of the NREL Phase II experimental wind turbine rotor is simulated to validate the developed BEM tool. The general characteristics of the NREL Phase II wind turbine are given in Table 3.6. The S809 blade profile is used for the entire blade. Experimental aerodynamic loads and planform data for this turbine are obtained from Reference [14]. These experimental lift and drag coefficients which are given in Figure 3.12, are measured in Delft wind tunnel for  $Re = 1 \times 10^6$  [14]. Power production of the NREL Phase II wind turbine is calculated and obtained results are compared with experimental results for different wind speeds in Figure 3.13. BEM analyses are performed with 17 blade sections and required aerodynamic loads are gathered from both the experiment and XFOIL potential solver. According to the obtained results, the BEM tool gives acceptable results. It is seen that, at low wind speeds, the solutions of BEM tool slightly differ. The reason behind is that flat plate approximation is used to obtain aerodynamic coefficients when sectional angle of attack is greater than  $20^\circ$ . At high wind speeds, BEM tool with experimental data agrees rather well with NREL Phase II test data while BEM + XFOIL slightly overpredicts the power production. These differences are all related to sectional angle of attack values and resulting lift and drag coefficients.

Table 3.6: Geometric characteristics of NREL phase II wind turbine.

Number of rotor blades	3
Airfoil profile	S809
Power control	Stall Control
Rotational speed	71.3 rpm
Rated Power	19.8 kW
Chord Length	0.4572 m
Root Extension	0.723 m
Diameter	10.06 m
Blade Set Angle	$12^\circ$
Twist	$0^\circ$

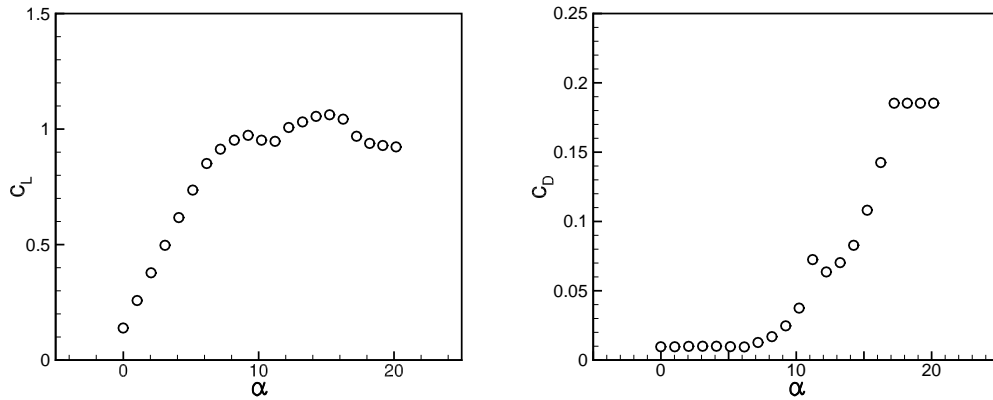


Figure 3.12: Experimental aerodynamic coefficients of S809 blade profile at  $Re = 1.0 \times 10^6$  [14].

### 3.3 Power Production Losses due to Icing

The ice accretion prediction tool developed is now integrated with the BEM methodology to predict power prediction losses for Aeolos-H 30kW wind turbine and NREL 5MW wind turbine.

#### 3.3.1 Aeolos-H 30kW wind turbine

Various icing events are simulated to see the effects of liquid water content, droplet diameter and temperature on the power production of the Aeolos-H 30kW wind turbine. The operating and icing conditions are shown in Table 3.7. In Figure 3.14, the obtained 2D iced profiles are extrapolated to generate 3D iced turbine blade. The accumulated ice develops along the blade span because of the increasing sectional velocity and decreasing sectional chord length.

Figures 3.15 – 3.17 show the variation of ice profiles along the blade for wind speeds 8.5 m/s, 11 m/s and 15 m/s respectively. It is observed that the predicted sectional ice shapes grow with the increasing radial position due to the increasing sectional velocity and the larger volume spanned by the blade section. As expected, the size of the accreted ice increases as the exposure time increases. In addition, as the wind

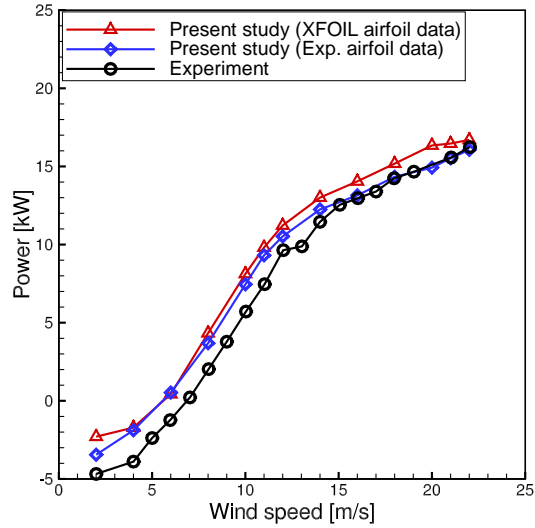


Figure 3.13: Test data and simulations comparison for NREL Phase II wind turbine [14].

Table 3.7: Parameters used to define icing profiles.

Blade profiles	DU93-W-210
Rotational speed	120 rpm
Rated speed	11 $m.s^{-1}$
Root chord	0.703 m
Tip chord	0.02 m
Turbine diameter ,R	12 m
Twist	17.45 degrees (max.)
Mode of control	variable speed/yawing
Free stream velocity, $V_{\infty}$	8.5 – 15 $m.s^{-1}$
Humidity	100 %
Liquid water content, LWC	0.05, 0.15, 0.25 $g/m^3$
Exposure time, $t_{exp}$	20 – 80 min
Droplet diameter, MVD	18, 27, 35 $\mu m$
Ambient temperature, $T_a$	-5.0, -10, -15 $^{\circ}C$
Ambient pressure, $p_{\infty}$	95610 Pa

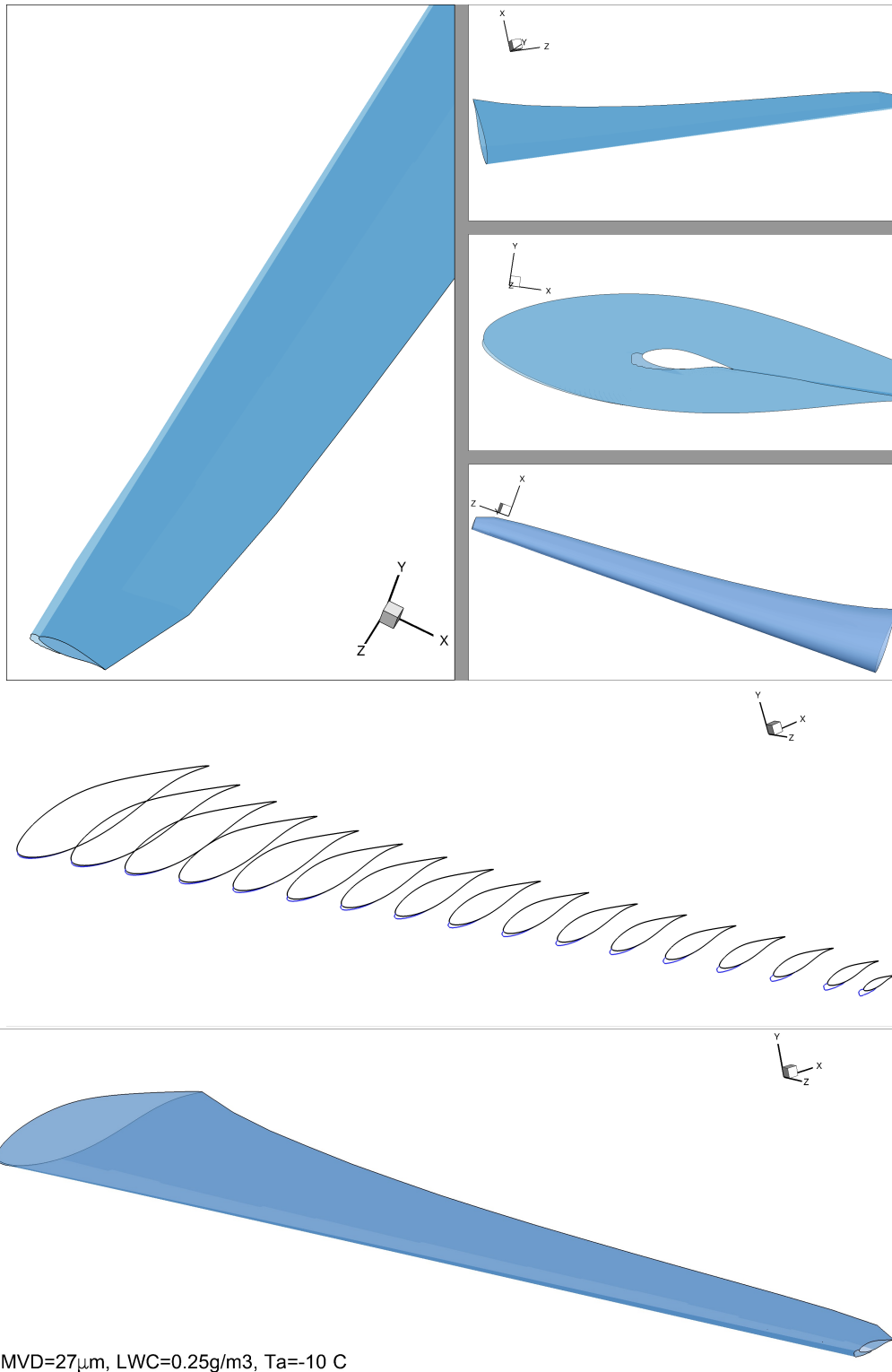


Figure 3.14: Predicted ice profiles for icing conditions given in Table 3.7 at the rated wind speed of 11m/s and 45min exposure time.

speed increases the ice tends to accumulate more at the pressure side of the blade.

The ice formations along the blade as the liquid water content, the droplet size and the temperature change at the rated wind speed of  $11\text{m/s}$  are all given in Figure 3.18. In the figures, the blade and ice profiles are non-dimensionalized with the local chord length. The results show that the ice volume at the leading edge of the blade, in general, increases along the span due to the fact that the spanned area by the blade exposed to impingement gets larger towards the blade tip. In addition, while the rime ice forms close to the hub, a glaze ice formation is mostly observed towards the tip. It is also observed that the variations in the droplet size and the temperature within the range considered in the present study do not affect the ice formation as much as the variation in the liquid water content.

The variation of the ice profiles along the blade span for the cases studied above at the rated wind speed and the variation of the rotor shaft power as a function of wind speed are given in Figure 3.19. The power curve demonstrates that as the relative wind speed increases along the blade span, the ice accretion similarly increases towards the tip and the ice occupies a larger percentage of the local chord. Such a qualitative prediction is in agreement with the most of the observations of iced rotor blades until the time the ice mass close to the tip breaks off [55, 42]. The corresponding power production curves for the clean and the iced wind turbines are given Figure 3.19b,d,f. It should be noted that the power production of the clean turbine predicted with the BEM tool is also in a good agreement with the experimental data (Figure 3.19b). It is again observed that the liquid water content has the most influence on the power loss. The power production losses predicted at the rated wind speed are in the range of 18 – 31%, which is in agreement with the numerical predictions reported in the literature [50, 37, 38, 39, 56]. Similar power losses are also reported by the wind farms [40, 41].

The power losses due to icing are next investigated as a function of exposure time. Figure 3.20 shows the ice accumulation on the blade and the distribution of power production along the blade span at the rated wind speed. As observed in the figure, the most of the power production occurs beyond the midspan location, where the relative velocities are larger. As the ice starts forming on the blade, the power production

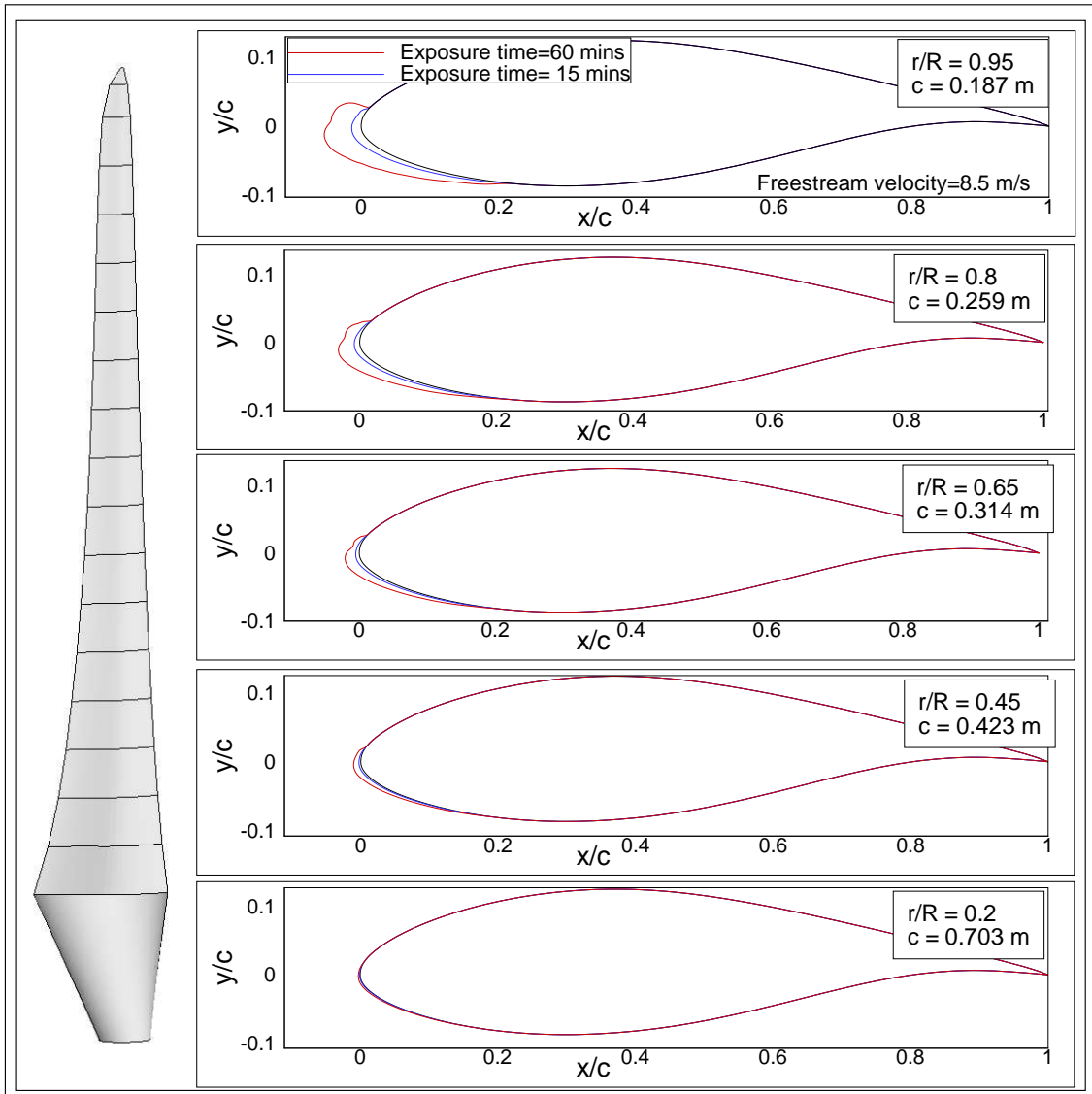


Figure 3.15: Predicted ice shapes for conditions in Table 3.7 at the wind speed of 8.5 m/s ( $LWC = 0.05 \text{ g/m}^3$ ,  $T_a = -10 \text{ }^\circ\text{C}$ ,  $MVD = 27 \mu\text{m}$ ).

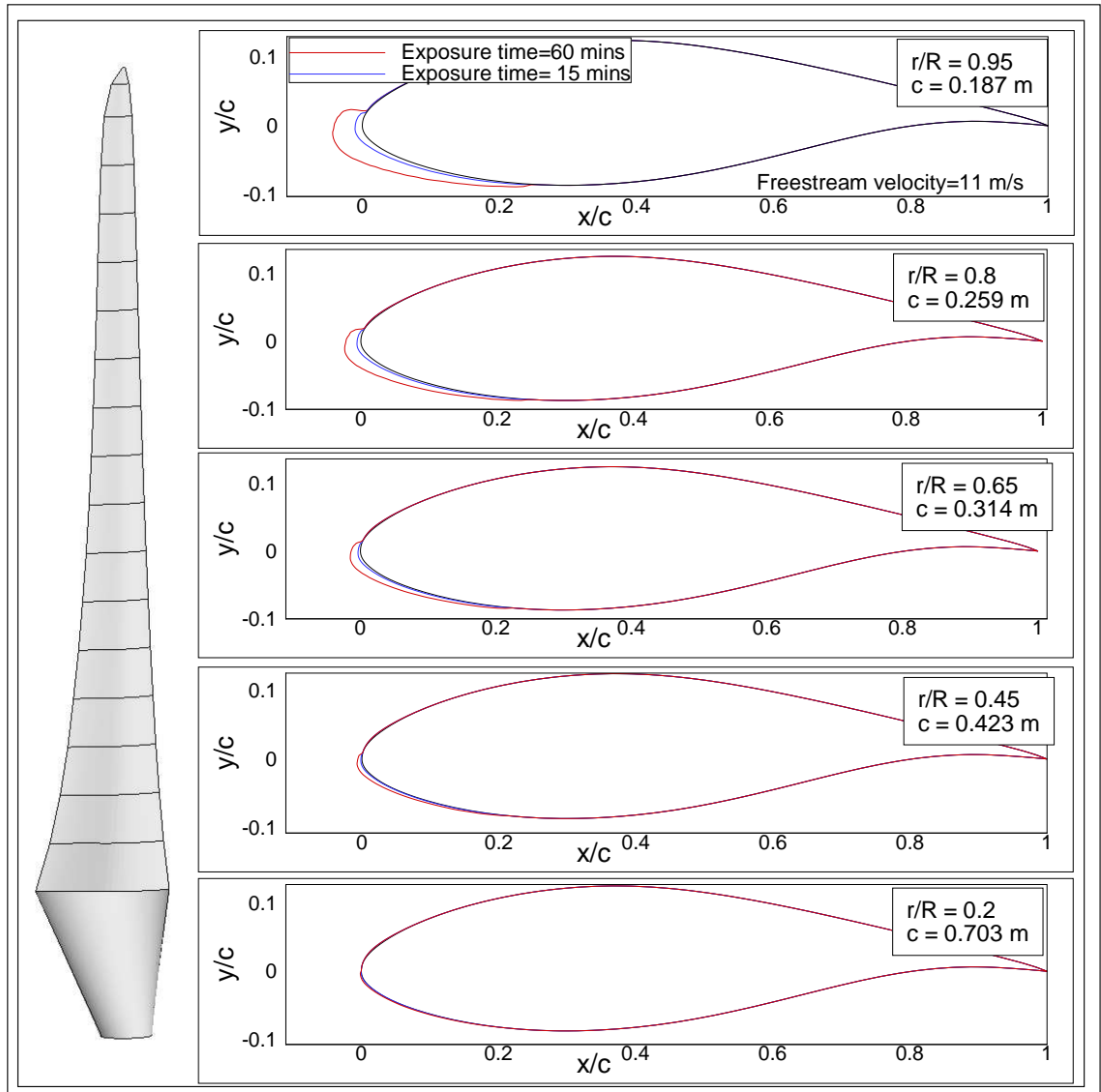


Figure 3.16: Predicted ice shapes for conditions in Table 3.7 at the rated wind speed of 11 m/s ( $LWC = 0.05 g/m^3$ ,  $T_a = -10^\circ C$ ,  $MVD = 27 \mu m$ ).

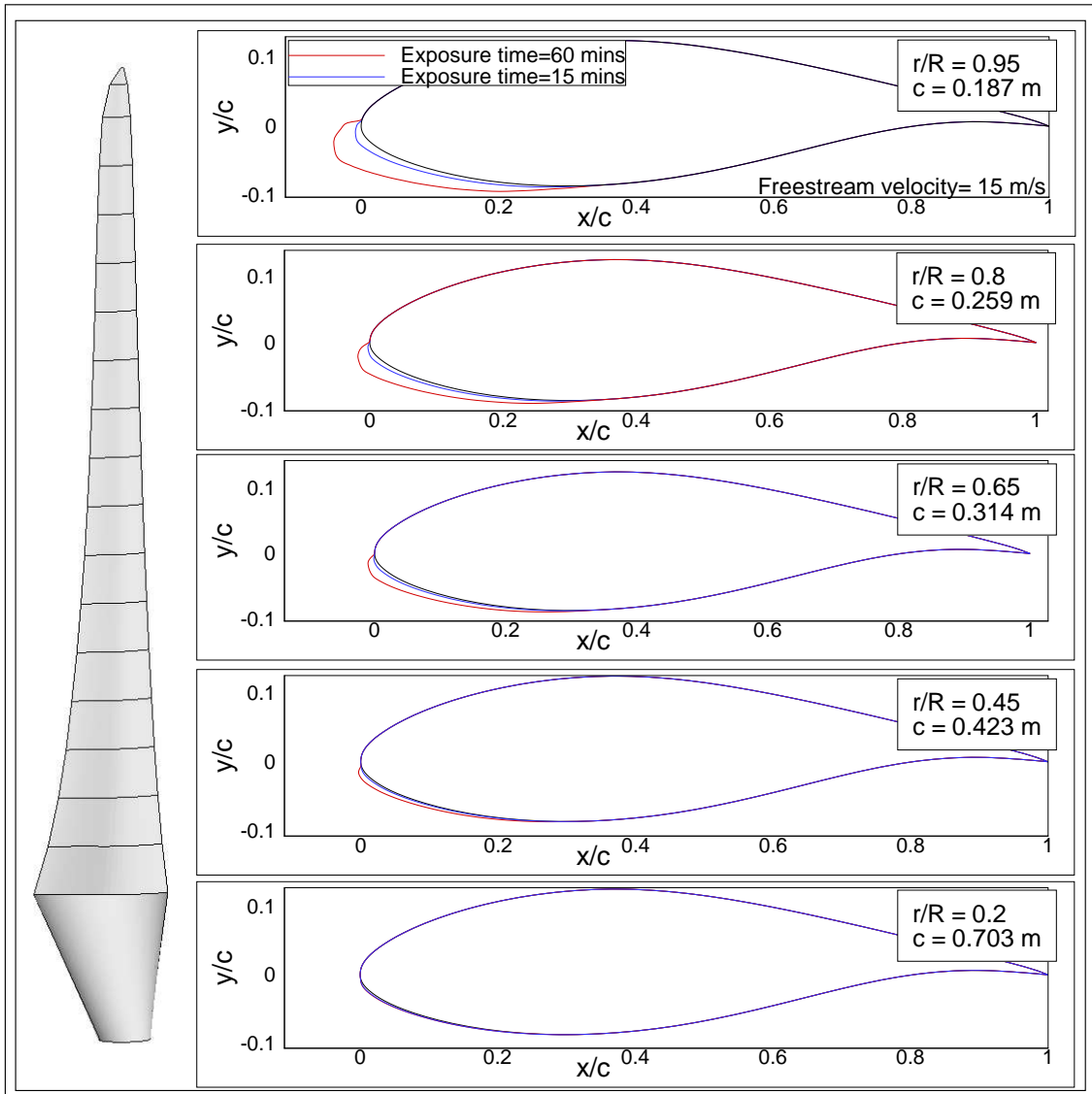
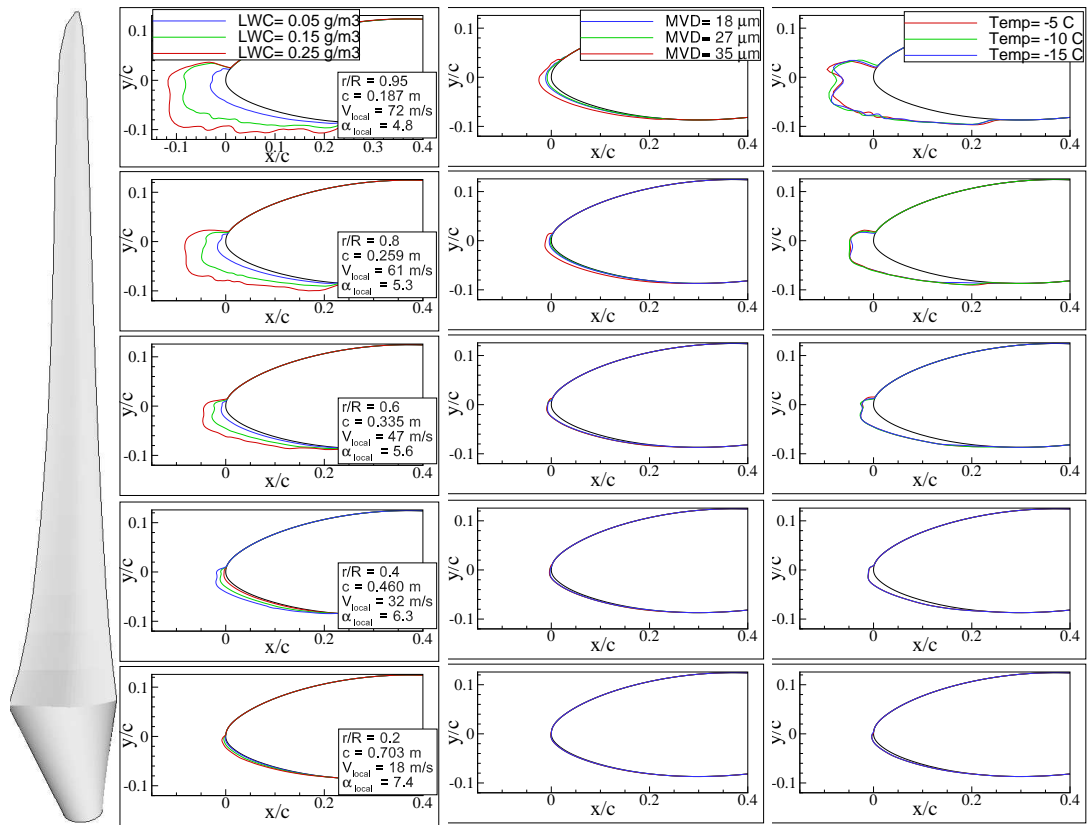
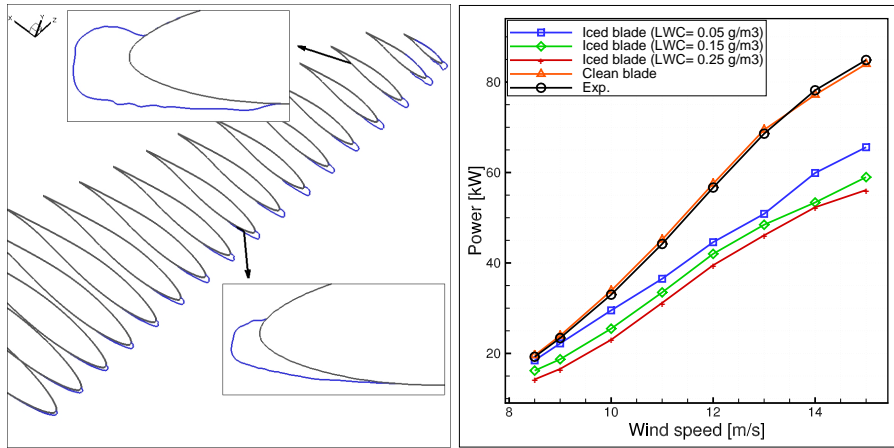


Figure 3.17: Predicted ice shapes for conditions in Table 3.7 at the wind speed of 15m/s ( $LWC = 0.05g/m^3$ ,  $T_a = -10\text{ }^\circ\text{C}$ ,  $MVD = 27\mu m$ ).

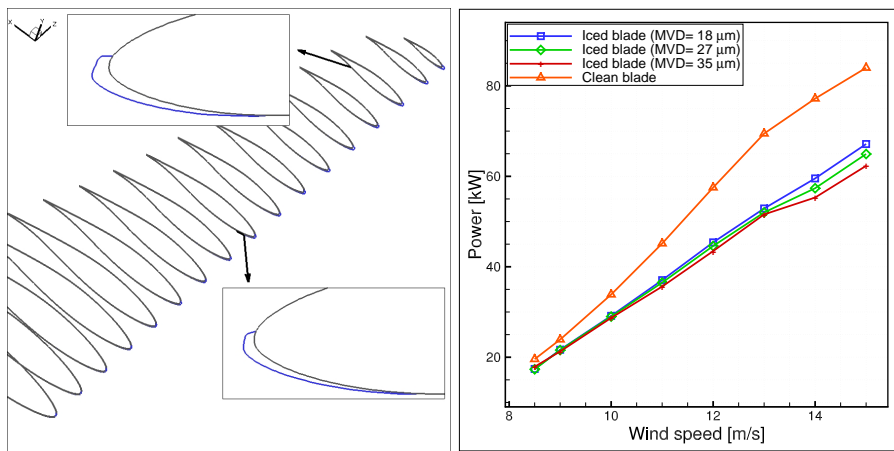


(a)  $MVD = 27\mu m, T_a = -10\text{ }^\circ C$       (b)  $LWC = 0.05g/m^3, T_a = -10\text{ }^\circ C$       (c)  $MVD = 27\mu m, LWC = 0.15g/m^3$

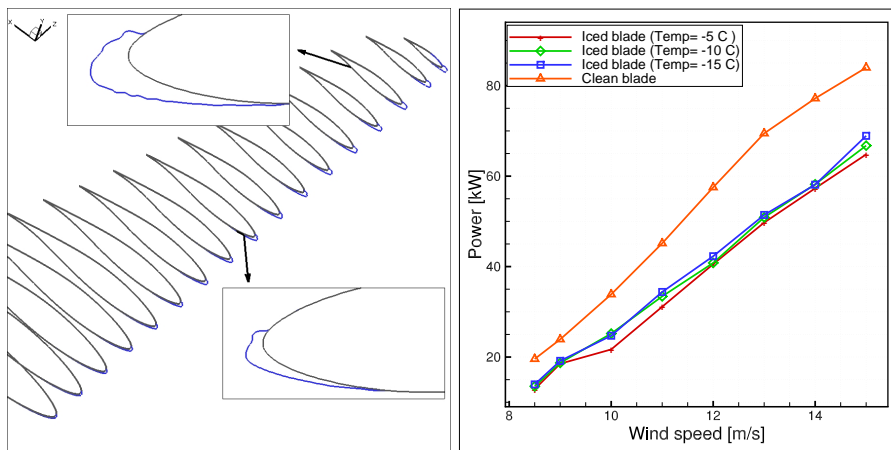
Figure 3.18: Predicted ice profiles for icing conditions given in Table 3.7 at the rated wind speed of  $11m/s$  and  $45min$  exposure time.



(a)  $LWC=0.25g/m^3, MVD=27\mu m, T_a=-10^\circ C$  (b) Power production and losses due to icing

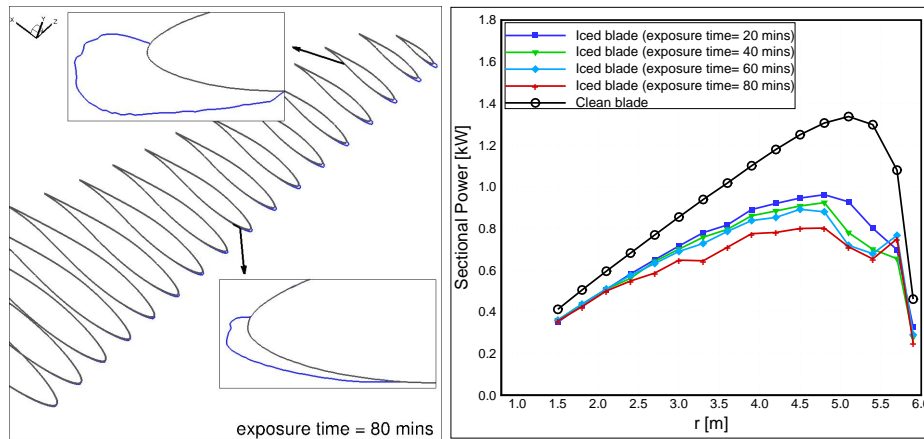


(c)  $LWC=0.05g/m^3, MVD=35\mu m, T_a=-10^\circ C$  (d) Power production and losses due to icing



(e)  $LWC=0.15g/m^3, MVD=27\mu m, T_a=-5^\circ C$  (f) Power production and losses due to icing

Figure 3.19: Predicted ice profiles over the blade at rated wind speed and power curve for 45min exposure time.



(a)  $LWC=0.15 \text{ g/m}^3$ ,  $MVD=27 \text{ }\mu\text{m}$ ,  $T_a = -10 \text{ }^\circ\text{C}$  (b) Sectional power production and pertained power losses

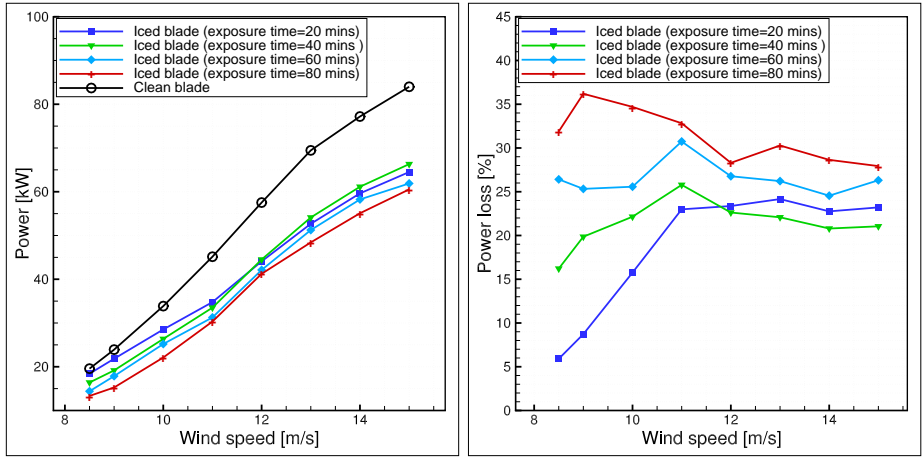
Figure 3.20: Predicted ice profiles over the blade and sectional power production at rated wind speed.

drops significantly along the blade span. As the exposure time increases, the power production keeps dropping over the blade but at a lower rate. It is also observed in Figure 3.20-b that close to the blade tip the power production does not drop as much. It is attributed to the relative increase in the local chord length due to icing, which contributes to the sectional power production.

The power production of the iced turbine and the percent power loss due to icing are given in Figure 3.21 as a function of exposure time and the wind speed. Similarly, the power production of the turbine drops rapidly as the ice forms within  $20\text{min}$  exposure time, then decreases gradually as the ice thickness increases at all wind speeds. The power loss at the rated wind speed and higher is observed to be in the range of 20 – 30% (Figure 3.21-b).

### 3.3.2 NREL 5MW wind turbine

Power production losses are next predicted for a large scale NREL 5MW wind turbine, which is formed by five different airfoil profiles along its span [57]. The icing condition considered is given in Table 3.8. The predicted rime ice profiles along the span are shown in Figure 3.23 and compared favorably against the predictions of



(a) Power curve and power losses with respect to exposure time (b) Percent power losses with respect to exposure time

Figure 3.21: Predicted power production and percent power loss for various icing exposure times.

Homola et al. [37] in Figure 3.22. The power production of the clean and the iced wind turbine at the wind speed of  $10\text{m/s}$  are evaluated to be  $3741\text{kW}$  and  $3111\text{kW}$  (17% loss) for the clean and iced turbine, respectively. Homola et al., who employ the FENSAP-ICE software for both flow field and ice accretion computations and an in-house BEM tool, predict  $3708\text{kW}$  and  $2800\text{kW}$  (24.5% loss) under the same icing conditions, but in their aerodynamic load computations they neglect the rotational effects and fix the Reynolds number. When the Reynolds number is fixed, the power production of the iced turbine with the present tool is evaluated to be  $2911\text{kW}$  (22.2% loss), which is in reasonable agreement.

### 3.4 Aerodynamic Shape Optimization to Reduce Power Losses due to Icing

In this section, the optimization of the blade profile around the leading edge is performed using three bump functions on each upper and lower surfaces, Figure 2.7. In the gradient vector evaluations, 30 min exposure to the atmospheric icing conditions at 11 m/s wind speed are considered. The blade profile is modified by a simple line search algorithm following the evaluation of the gradient vector. The evaluation of the gradient vector and the modification of the blade profile continue until the change

Table 3.8: Properties of NREL 5MW wind turbine and atmospheric icing conditions.

Blade profiles	DU 40, DU 25, DU 21, NACA 64618 $\times$ 2 (Sec. A-E)
Rotational speed	12.1 rpm
Rated speed	11.4 $m.s^{-1}$
Root chord	4.557 m
Tip chord	1.419 m
Turbine diameter ,R	63 m
Twist	13.308 degrees (max.)
Liquid water content, LWC	0.22 $g/m^3$
Droplet diameter, MVD	20 $\mu m$
Ambient temperature, $T_a$	-10 $^{\circ}C$
Ambient pressure, $p_{\infty}$	95610 Pa
Humidity	100 %

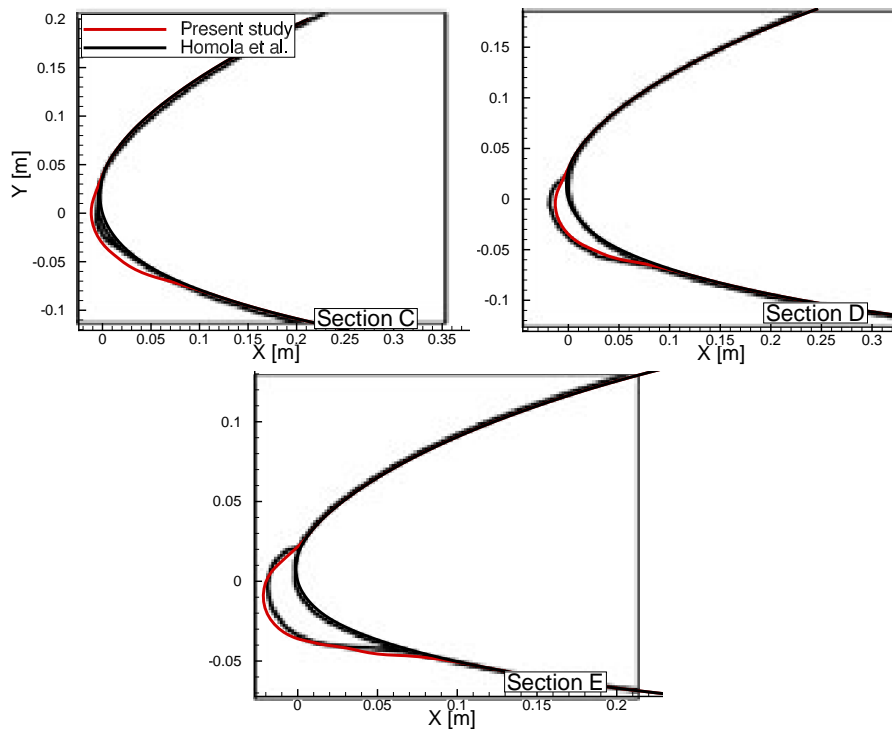


Figure 3.22: Predicted ice shapes at 10  $m/s$  for NREL 5MW wind turbine under icing conditions in Table 3.8.

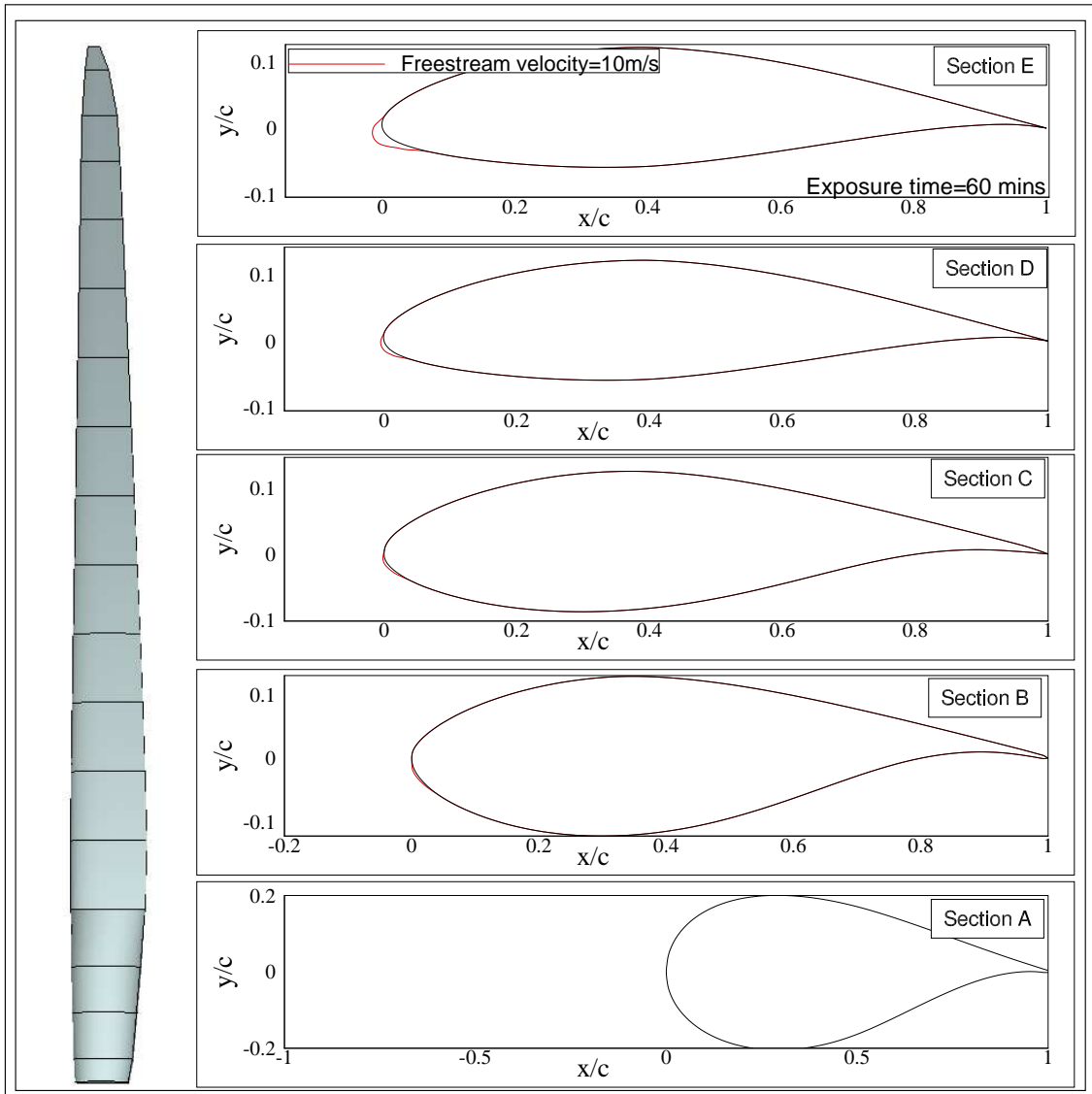


Figure 3.23: Predicted ice shapes for conditions in Table 3.8 at the wind speed of  $10\text{m/s}$ .

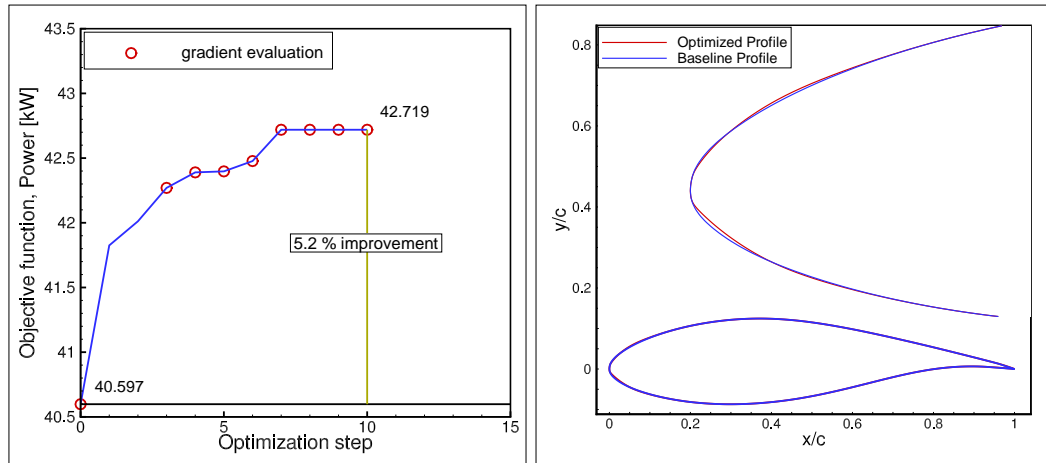


Figure 3.24: Bump functions (left), Aeolos wind turbine baseline blade profile (DU93-W-210) and the optimized profile (right).

in power production is less than 0.1%. The optimized blade profile is given in Figure 3.24.

The predicted ice shapes for the baseline and the optimized profiles corresponding to the 30 minutes exposure time are given in Figure 3.25. As seen, the ice shapes have a similar trend for both the baseline and optimized blade profiles near the root section. After the midspan, the predicted ice shapes start to diverge, and on the baseline blade profile the ice shapes which are formed have more irregularity than the optimized blade profile. As expected, the ice mass increases, as the inflow velocity increases along the blade span with maximum velocity at the tip reaching 0.3 Mach. Therefore, the ice accumulation increases along the span and the maximum ice accretion forms at the blade tip. The exposure time is the most critical parameter for icing. It should be noted that the optimized blade profile has a smoother ice shape on the upper side of the leading edge, which should be responsible for the improved aerodynamic performance of the iced blade by further delaying leading edge flow separation.

In Figure 3.26-a the computed power production of the Aeolos wind turbine is given for both the baseline and the optimized blade profiles for 30 min exposure time. It should be noted that the optimization is performed at the rated wind speed of 11  $m/s$ . While the optimized clean blade profile produces about the same power as the baseline profile at 11  $m/s$ , it produces more power for all exposure times and at all wind speeds considered. The power loss of the optimized blade profile is 3.8% less

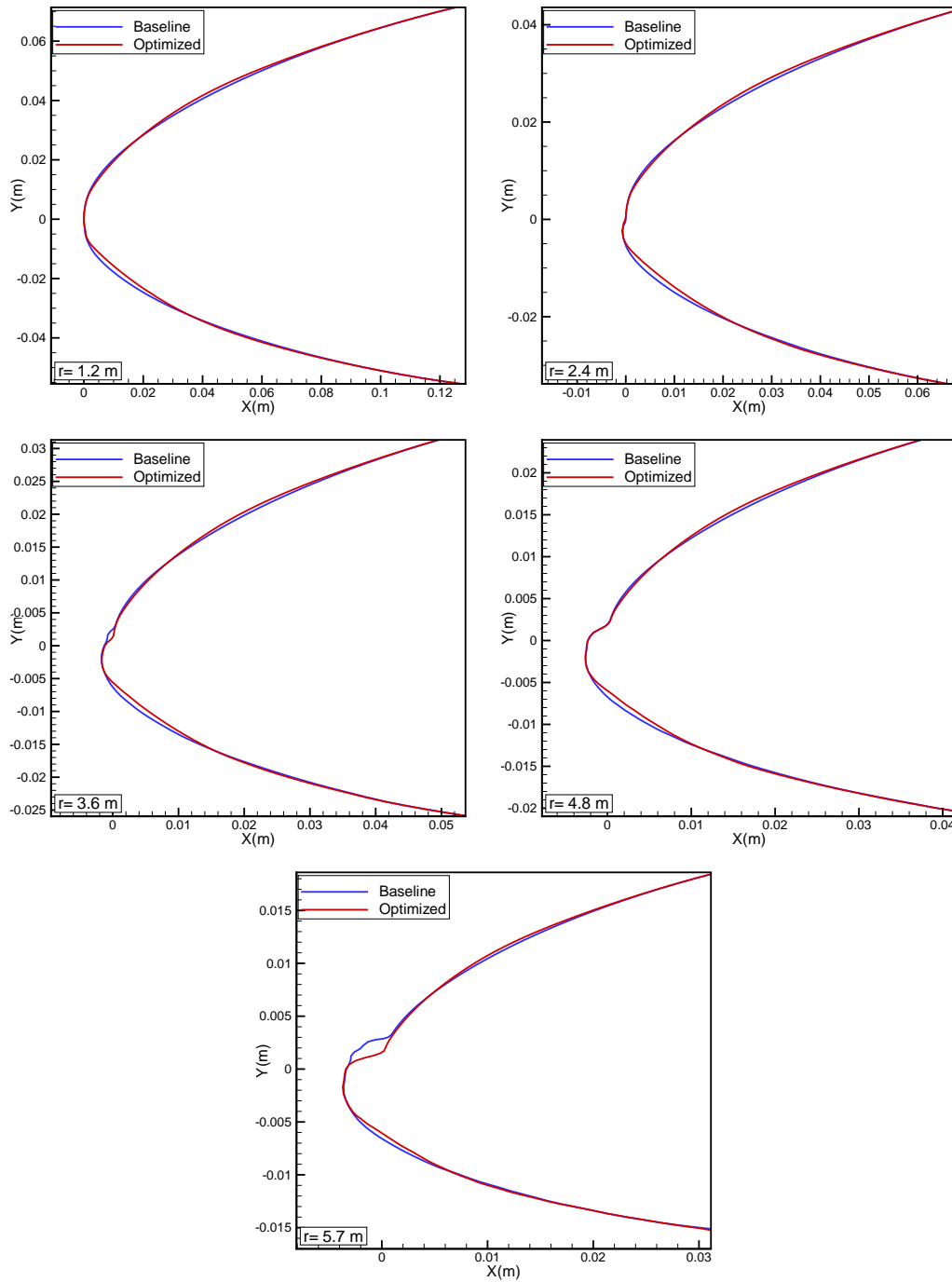
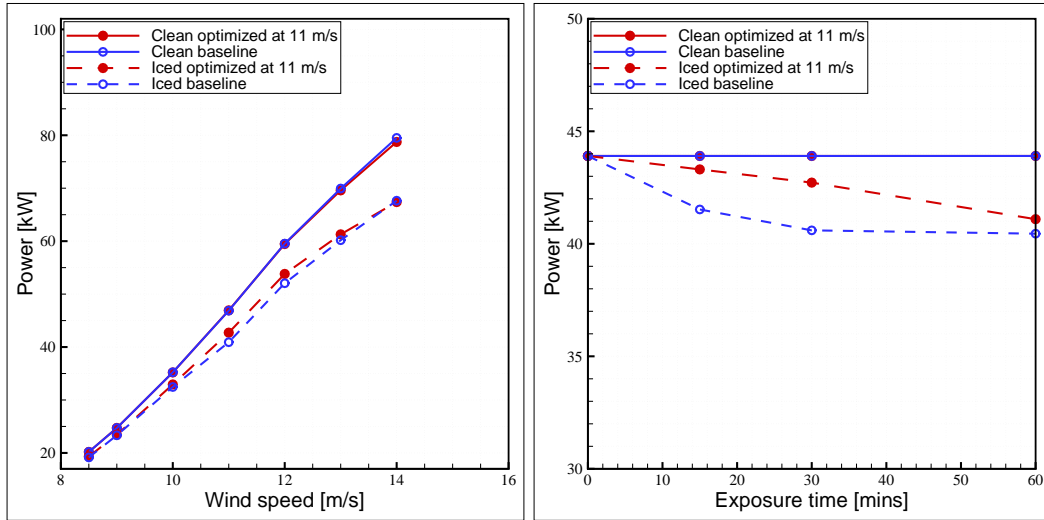


Figure 3.25: Predicted ice profiles for baseline and optimized blade profiles at rated wind speed ( $LWC=0.05g/m^3$ ,  $MVD=18\mu m$ ,  $T_a=-10^\circ C$ ).



(a) Power production curve for 30 mins exposure time (b) Power production curve at 11 m/s wind speed with respect to icing time

Figure 3.26: Power production of Aeolos 30 kW wind turbine.

than the baseline profile at 11  $m/s$  and 30min exposure time. In Figure 3.26-b, the power production of the optimized blade profile is compared to that of the baseline profile as a function of exposure time. Although the shape optimization is performed for 30min exposure time, a reduction in the power production loss is observed at all exposure times. But the improvement diminishes as the exposure time increases.



## CHAPTER 4

### CONCLUSION

In this thesis, an efficient methodology is developed for the prediction of ice accretion on wind turbine blades under various atmospheric icing conditions and the consequent power production losses. A gradient based optimization algorithm is successfully coupled into this methodology in order to perform aerodynamic shape optimization of blade profiles for minimizing the power production losses due to icing. It is shown that the Extended Messinger icing model coupled with the BEM tool performs well for rime ice and glime (mild glaze) ice accretions both in terms of the ice thickness and related power losses. The BEM tool employs XFOIL, which is a 2D flow solver with a turbulent transition model. It provides a fast performance, and ease of use for ice accretion predictions and performance losses. Various icing events as a function of the liquid water content, droplet diameter, temperature and exposure time are simulated for the Aeolos-H 30 kW and NREL 5MW wind turbines. The power production losses under the concurrent rime and glaze ice formations are successfully predicted. For an exposure time of 1 hour, the power loss predicted could be as much as 30%.

Aerodynamic shape optimization studies are performed for minimizing power production losses under icing conditions, In an optimization study performed for 30min exposure time at the rated wind speed, the power loss due to icing is reduced by about 4% while keeping the power production about the same for the clean profile. The optimized blade profile causes a smoother ice shape on the upper side of the leading edge, which slightly delays the leading edge flow separation and improves the aerodynamic performance. The preliminary results obtained are encouraging and it is suggested that the shape optimization should be performed at various sections along the blade span independently to further reduce the power production losses.

It is shown that the present ice accretion and power production estimation tool developed is accurate, efficient and cost effective. It may therefore be effectively used in order to estimate rime, glime and mild glaze ice formations on wind turbine blades under various icing conditions and the corresponding power production losses. It may also be employed in the design of electro-thermal or hot air flow anti/de-icing systems. Future work is needed to predict power production losses more accurately under heavy glaze ice conditions by using a Navier-Stokes solver such as SU2. Accurate predictions of icing related losses and the blade optimization performed in this study are expected to be a supportive contribution during the design process of wind turbines.

## REFERENCES

- [1] Rho Shin Myong. Atmospheric icing effects on aerodynamics of wind turbine blade. In *ASME 2013 International Mechanical Engineering Congress and Exposition*, pages V07BT08A072–V07BT08A072. American Society of Mechanical Engineers, 2013.
- [2] R Cattin and DU Heikkilä. Evaluation of ice detection systems for wind turbines. *VGB Research Project*, (392), 2016.
- [3] Lorenzo Battisti. *Wind turbines in cold climates: Icing impacts and mitigation systems*. Springer, 2015.
- [4] R Cattin. Validation of the IEA Task 19 ice site classification. *Winterwind 2016*, 2016.
- [5] Yiqiang Han. *Theoretical and Experimental Study of Scaling Methods for Rotor Blade Ice Accretion Testing*. PhD thesis, Pennsylvania State University, 2011.
- [6] B Tammelin, A Böhlinger, M Cavaliere, H Holttinen, C Morgan, H Seifert, et al. Wind energy production in cold climate (weco). final report 1 January 1996 to 31 December 1998. 2000.
- [7] Saturday silliness–wind turbine photo of the year. <https://wattsupwiththat.com/2016/01/23/saturday-silliness-wind-turbine-photo-of-the-year/>. (Accessed on 03/25/2018).
- [8] Frank T Lynch and Abdollah Khodadoust. Effects of ice accretions on aircraft aerodynamics. *Progress in Aerospace Sciences*, 37(8):669–767, 2001.
- [9] Ping Fu and Masoud Farzaneh. A CFD approach for modeling the rime-ice accretion process on a horizontal-axis wind turbine. *Journal of Wind Engineering and Industrial Aerodynamics*, 98(4-5):181–188, 2010.

- [10] Thomas Reid, Guido Baruzzi, Isik Ozcer, David Switchenko, and Wagdi Habashi. Fensap-ice simulation of icing on wind turbine blades, part 1: performance degradation. In *51st AIAA Aerospace Sciences Meeting including the New Horizons Forum and Aerospace Exposition*, page 750, 2013.
- [11] S Barber, Y Wang, S Jafari, N Chokani, and RS Abhari. The effect of icing on wind turbine performance and aerodynamics. In *EWEC*, 2010.
- [12] Egemen Ogretim, Wade W Huebsch, and Aaron Shinn. Aircraft ice accretion prediction based on neural networks. *Journal of aircraft*, 43(1):233–240, 2006.
- [13] Yiqiang Han, Jose Palacios, and Sven Schmitz. Scaled ice accretion experiments on a rotating wind turbine blade. *Journal of Wind Engineering and Industrial Aerodynamics*, 109:55 – 67, 2012.
- [14] JG Schepers, AJ Brand, A Bruining, M Hand, D Infield, H Madsen, T Maeda, J Paynter, R van Rooij, Y Shimizu, et al. Final report of IEA Annex XVIII: enhanced field rotor aerodynamics database. *Energy Research Center of the Netherlands, ECN-C-02-016, February*, 2002.
- [15] Navigant Research. World market update 2013. <http://www.navigantresearch.com/research/world-market-update-2013>. (Accessed on 03/15/2016).
- [16] William J Jasinski, Shawn C Noe, Michael S Selig, and Michael B Bragg. Wind turbine performance under icing conditions. *Journal of Solar Energy Engineering*, 120(1):60–65, 1998.
- [17] N Dalili, A Edrissy, and R Carriveau. A review of surface engineering issues critical to wind turbine performance. *Renewable and Sustainable Energy Reviews*, 13(2):428–438, 2009.
- [18] JG Pallarol, Bengt Sundén, and Zan Wu. On ice accretion for wind turbines and influence of some parameters. *Aerodynamics of Wind Turbines: Emerging Topics*, 2014.
- [19] RW Gent, NP Dart, and JT Cansdale. Aircraft icing. *Philosophical Transactions of the Royal Society of London A: Mathematical, Physical and Engineering Sciences*, 358(1776):2873–2911, 2000.

- [20] Matthew Carl Homola. Impacts and causes of icing on wind turbines. *Navrik University College Report*, 2005.
- [21] Greg Weston. Northern new brunswick wind turbines frozen solid. <http://www.nationalpost.com/Northern+Brunswick+wind+turbines+frozen+solid/4287063/story.html>. (Accessed on 03/25/2018).
- [22] L Talhaug, K Vindteknik, G Ronsten, R Horbaty, I Baring-Gould, A Lacroix, and E Peltola. Wind energy projects in cold climates. *Executive Committee of the International Energy Agency Program for Research and Development on Wind Energy Conversion Systems*, pages 1–36, 2005.
- [23] L Talhaug, K Vindteknik, G Ronsten, R Horbaty, I Baring-Gould, A Lacroix, and Esa Peltola. Wind energy projects in cold climates. [http://virtual.vtt.fi/virtual/arcticwind/06\\_JFC\\_Icing\\_losses\\_20110401.pdf](http://virtual.vtt.fi/virtual/arcticwind/06_JFC_Icing_losses_20110401.pdf). (Accessed on 03/11/2015).
- [24] Timo Laakso, H Holttinen, G Ronsten, L Tallhaug, R Horbaty, I Baring-Gould, A Lacroix, E Peltola, and B Tammelin. State-of-the-art of wind energy in cold climates. *IEA annex XIX*, 24, 2003.
- [25] Guy Fortin, Jean Perron, and Adrian Ilinca. Behaviour and modeling of cup anemometers under icing conditions. *IWAIS XI, Montréal, Canada*, 6, 2005.
- [26] Guy Fortin and Jean Perron. Wind turbine icing and de-icing. In *47th AIAA Aerospace Sciences Meeting*, 2009.
- [27] Olivier Parent and Adrian Ilinca. Anti-icing and de-icing techniques for wind turbines: Critical review. *Cold regions science and technology*, 65(1):88–96, 2011.
- [28] Bernard L. Messinger. Equilibrium temperature of an unheated icing surface as a function of air speed. *Journal of the Aeronautical Sciences*, 20(1):29–42, 1953.
- [29] Tim G Myers. Extension to the messinger model for aircraft icing. *AIAA journal*, 39(2):211–218, 2001.

- [30] S Özgen and M Canbek. Ice accretion simulation on multi-element airfoils using extended messinger model. *Heat and Mass Transfer*, 45(3):305, 2009.
- [31] Adriána Hudecz, Holger Koss, and Martin OL Hansen. Ice accretion on wind turbine blades. *Proceedings of the IWAIS, Newfoundland and Labrador, Sept*, pages 8–11, 2013.
- [32] GM Ibrahim, K Pope, and YS Muzychka. Effects of blade design on ice accretion for horizontal axis wind turbines. *Journal of Wind Engineering and Industrial Aerodynamics*, 173:39–52, 2018.
- [33] Edward W Brouwers, Jose L Palacios, Edward C Smith, and Andrew A Peterson. The experimental investigation of a rotor hover icing model with shedding. In *American Helicopter Society 66th Annual Forum*, pages 1863–1875, 2010.
- [34] Wei Yu, Ming Ming Zhang, and Jian Zhong Xu. Effect of smart rotor control using a deformable trailing edge flap on load reduction under normal and extreme turbulence. *Energies*, 5(9):3608–3626, 2012.
- [35] Lichun Shu, Jian Liang, Qin Hu, Xingliang Jiang, Xiaokai Ren, and Gang Qiu. Study on small wind turbine icing and its performance. *Cold Regions Science and Technology*, 134:11–19, 2017.
- [36] S Barber, Y Wang, N Chokani, and RS Abhari. The effect of ice shapes on wind turbine performance. In *13th International Workshop on Atmospheric Icing of Structures, Andermatt, Switzerland*, 2009.
- [37] Matthew C. Homola, Muhammad S. Virk, Per J. Nicklasson, and Per A. Sundsbø. Performance losses due to ice accretion for a 5 mw wind turbine. *Wind Energy*, 15(3):379–389, 2012.
- [38] Matthew C Homola, Muhammad S Virk, Per J Nicklasson, and PA Sundsbø. Modelling of ice induced power losses and comparison with observations. *Proceedings of the Winterwind*, 2011.
- [39] MT Brahim, D Chocron, and I Paraschivoiu. Prediction of ice accretion and performance degradation of hawt in cold climates. *AIAA Paper*, (98-0026), 1997.

- [40] Erik Rindeskär. Modelling of icing for wind farms in cold climate. *Department of Earth Sciences, Uppsala University: Uppsala, Sweden*, 2010.
- [41] Daniel Gillenwater, Christian Masson, and Jean Perron. Wind turbine performance during icing events. In *Proceedings of the 46th AIAA Aerospace Sciences Meeting and Exhibit, AIAA-2008*, volume 1344, 2008.
- [42] S Barber, Y Wang, S Jafari, N Chokani, and RS Abhari. The impact of ice formation on wind turbine performance and aerodynamics. *Journal of Solar Energy Engineering*, 133(1):011007, 2011.
- [43] Drela Mark. [web.mit.edu/drela/public/web/xfoil/](http://web.mit.edu/drela/Public/web/xfoil/). <http://web.mit.edu/drela/Public/web/xfoil/>. (Accessed on 04/24/2018).
- [44] I Paraschivou and F Saeed. Aircraft icing (unpublished book draft). 2007.
- [45] Guy Fortin, Jean-Louis Laforte, and Adrian Ilinca. Heat and mass transfer during ice accretion on aircraft wings with an improved roughness model. *International Journal of Thermal Sciences*, 45(6):595 – 606, 2006.
- [46] Gabriel Taubin. Curve and surface smoothing without shrinkage. In *Computer Vision, 1995. Proceedings., Fifth International Conference on*, pages 852–857. IEEE, 1995.
- [47] Raymond Morton Hicks, Earll M Murman, and Garret N Vanderplaats. An assessment of airfoil design by numerical optimization. 1974.
- [48] Raymond M Hicks and Preston A Henne. Wing design by numerical optimization. *Journal of Aircraft*, 15(7):407–412, 1978.
- [49] LEWICE. Nasa glenn research center. <https://www1.grc.nasa.gov/aeronautics/icing/software/>. (Accessed on 06/24/2018).
- [50] Peter Blasco, Jose Palacios, and Sven Schmitz. Effect of icing roughness on wind turbine power production. *Wind Energy*, 20(4):601–617, 2017. we.2026.
- [51] Matthew C Homola, Muhammad S Virk, Tomas Wallenius, Per J Nicklasson, and Per A Sundsbø. Effect of atmospheric temperature and droplet size variation on ice accretion of wind turbine blades. *Journal of wind engineering and industrial aerodynamics*, 98(12):724–729, 2010.

- [52] Lasse Makkonen, Timo Laakso, Mauri Marjaniemi, and Karen J Finstad. Modelling and prevention of ice accretion on wind turbines. *Wind Engineering*, 25(1):3–21, 2001.
- [53] SU2. Su2. <https://su2code.github.io/>. (Accessed on 08/24/2018).
- [54] Francisco Palacios, Juan Alonso, Karthikeyan Duraisamy, Michael Colonno, Jason Hicken, Aniket Aranake, Alejandro Campos, Sean Copeland, Thomas Economon, Amrita Lonkar, et al. Stanford university unstructured (su 2): an open-source integrated computational environment for multi-physics simulation and design. In *51st AIAA Aerospace Sciences Meeting including the New Horizons Forum and Aerospace Exposition*, page 287, 2013.
- [55] B Tammelin, M Cavaliere, H Holttinen, C Morgan, H Seifert, and K Säntti. Wind energy production in cold climate (weco). finnish meteorological institute rep. Technical report, JOR3-CT95-0014, 38 pp.[Available online at <http://cordis.europa.eu/documents/documentlibrary/47698271EN6.pdf>], 2000.
- [56] M. Etemaddar, M. O. L. Hansen, and T. Moan. Wind turbine aerodynamic response under atmospheric icing conditions. *Wind Energy*, 17(2):241–265, 2014.
- [57] Jason Jonkman, Sandy Butterfield, Walter Musial, and George Scott. Definition of a 5-mw reference wind turbine for offshore system development. *National Renewable Energy Laboratory, Golden, CO, Technical Report No. NREL/TP-500-38060*, 2009.

## Appendix A

### ICING SEVERITY

The icing event is a critical natural phenomena and probabilistic concept for the assessment of the economic influence of icing on WECSs operating in wind farms with a certain ice risk. The icing event depends on a certain subset of conditions determined by the intersection area illustrated in Figure A.1.

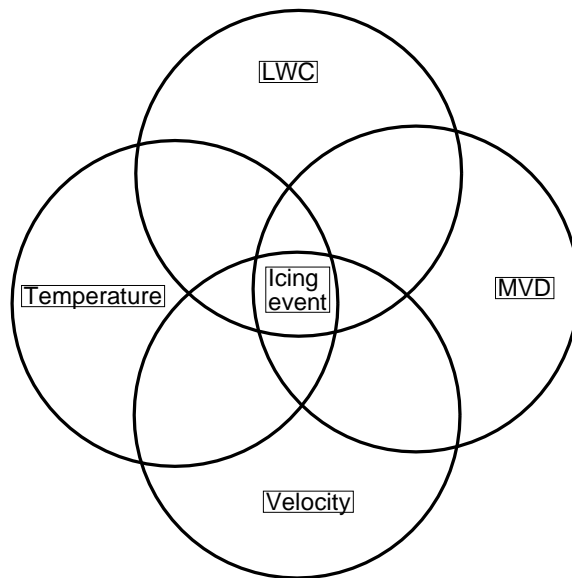


Figure A.1: Definition of the icing event.

IEA Ice Classification ensures a first pointer on the severity of icing and its consequences for a given site and can be seen in Table A.1.

Table A.1: IEA ice classification with corresponding recommendations (Reprinted from Ref [4]).

IEA Ice class	Meteorological icing (% of year)	Instrumental icing (% of year)	Production loss (% of annual production)
5 (heavy)	>10	>20	>20
4 (strong)	5–10	10–30	10–25
3 (moderate)	3–5	6–15	3–12
2 (light)	0.5–3	1–9	0.5–5
1 (occasional)	0–0.5	<1.5	0–0.5

Meteorological icing is the time when icing weather conditions are present and instrumental icing is the time when ice is present on instruments, components, or other structures.

## Appendix B

### AERODYNAMIC STALL

The lift force usually increases with the angle until the critical angle of attack (i.e. stall angle) and it drops dramatically. This physical phenomenon is called aerodynamic stall.

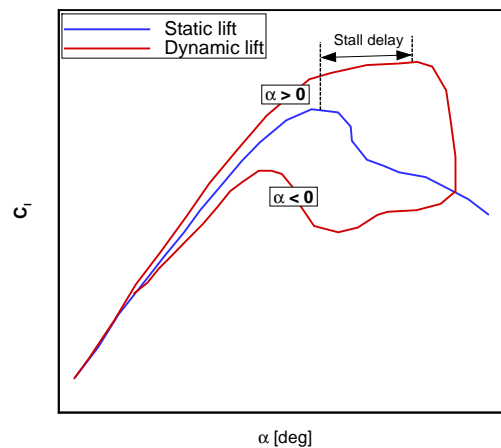


Figure B.1: A representative schematic diagram of lift under static and dynamic changes in the angle of attack.

#### B.1 Static Stall

In steady flow, when the angle of attack changes slowly in a fixed wing aircrafts static stall (flow separation) occurs. In this case, the lift coefficient is a direct function of the angle of attack as shown in Figure B.1 until the stall.

## B.2 Dynamic Stall

In a wind turbine blade, the angle of attack changes rapidly due to rotation, pitching motion and the vibrations of the blade. Rapid variations in angle of attack make lift force history dependent since there is a periodic lift force curve between increasing and decreasing angles of attack in turbine blades (hysteresis produced), as shown in Figure B.2. The two important effects of dynamic stall are stall delay and overshoot of the lift force, and are summarized as follows:

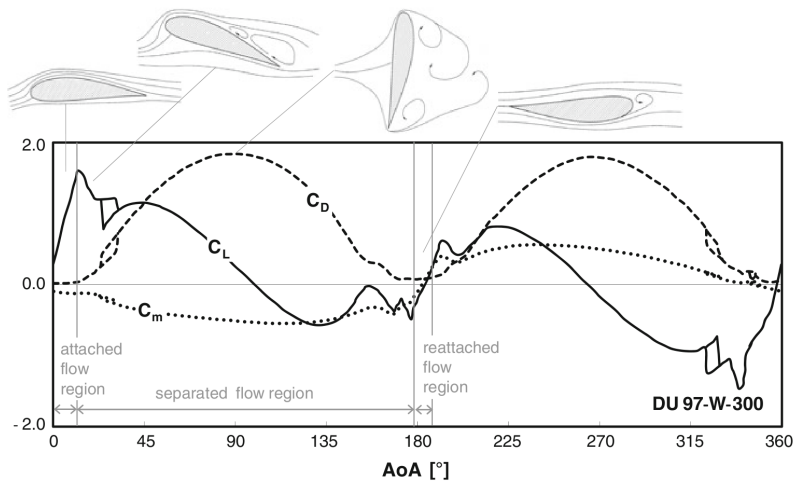


Figure B.2: A typical hysteresis loop for a wind turbine blade profile [3].

### B.2.1 Stall Delay

A turbine blade with a positive rate of angle of attack (upstroke) stalls at an angle of attack greater than the static stall angle. The stall recovery (reattachment) during a negative rate of angle of attack (downstroke) usually occurs at an angle less than the static stall angle.

### B.2.2 Overshoot of the Lift Force

The lift forces are quite higher than those for the static counterparts. This affects stresses and the fatigue life of the turbine blade.

## CURRICULUM VITAE

### PERSONAL INFORMATION

**Surname, Name:** YIRTICI, Ozcan

**Nationality:** Turkish (TC)

**Date and Place of Birth:** 25.09.1984, Antakya

**Marital Status:** Single

**Phone:** +90 5552057641

**E-mail:** oyirtici@ae.metu.edu.tr, ozcanyirtici@gmail.com

### EDUCATION

<b>Degree</b>	<b>Institution</b>	<b>Year of Graduation</b>
M.S.	METU Aerospace Engineering	2012
B.S.	Çukurova University, Department of Physics	2006
High School	Nihal Turgut Anlar Anadolu Öğretmen Lisesi	2002

### ACADEMIC EXPERIENCE

<b>Year</b>	<b>Place</b>	<b>Enrollment</b>
2008 - Present	METU Aerospace Engineering	Graduate Research Asistant

### RESEARCH INTERESTS

Icing, Ice Accretion, CFD, Parallel Computing, Turbulent Flow, Wind Energy

## **FOREIGN LANGUAGES**

Advanced English

## **JOURNAL ARTICLES**

1. Özcan YIRTICI, Serkan ÖZGEN and İsmail Hakkı TUNCER, Predictions of ice formations on wind turbine blades and power production losses due to icing, WIND ENERGY (under review)

## **INTERNATIONAL CONFERENCE PAPERS**

1.Özcan YIRTICI, Tansu SEVİNE, Serkan ÖZGEN and İsmail Hakkı TUNCER, Wind Turbine Performance Losses Due to the Ice Accretion on the Turbine Blades, 2018 Joint Thermophysics and Heat Transfer Conference, Atlanta, Georgia, 25-29 June, 2018. (AIAA 2018-4291)

2. Özcan YIRTICI, Serkan ÖZGEN and İsmail Hakkı TUNCER, Aerodynamic Shape Optimization of Wind Turbine Blades for Reducing Icing Related Power Losses, 26th Annual Conference of the CFD Society of Canada, Winnipeg, Manitoba, June 10-12, 2018.

3. Özcan YIRTICI, Kenan CENGİZ and İsmail Hakkı TUNCER, Performance Degradation Analysis of an Iced Turbine Blade by Using Detached-Eddy Simulation, Proceedings of Parallel CFD 2018, Indianapolis, Indiana, May 14-17, 2018.

4. Özcan YIRTICI, İsmail Hakkı TUNCER and Serkan ÖZGEN, Icing on Wind Turbine Blade under Various Atmospheric Conditions, 9th AIAC, number 179, Ankara, September, 2017

5. Özcan YIRTICI, İsmail Hakkı TUNCER and Serkan ÖZGEN, Aerodynamic Shape Optimization of Wind Turbine Blades for Reducing Power Production Losses due to Ice Accretion, 35th Wind Energy Symposium, Texas, January 2017.

6. Özcan YIRTICI, İsmail Hakkı TUNCER and Serkan ÖZGEN, Ice Accretion Prediction on Wind Turbines and Consequent Power Losses, Journal of Physics: Conference Series, Volume 753, Issue 2, article id. 022022, 2016.
7. Serkan ÖZGEN, Özcan YIRTICI and İsmail Hakkı TUNCER, Ice Accretion Prediction on Horizontal Axis Wind Turbine Blades, 8th AIAC, number 163, Ankara, September, 2015
8. Özcan YIRTICI, Serkan ÖZGEN and İsmail Hakkı TUNCER, Aerodynamic Performance Losses due to Ice Buildup in Wind Turbines, EAWE 10th PhD Seminar on Wind Energy in Europe, Orleans, France, October 28-31, 2014.
9. Özcan YIRTICI and İsmail Hakkı TUNCER, Parallel Implementation of Detached Eddy Simulation on 2D Hybrid Grids, 7th AIAC, number 162, Ankara, September, 2013.

#### **NATIONAL CONFERENCE PAPERS**

1. Özcan YIRTICI Serkan Özgen and İsmail Hakkı TUNCER, Buzlanmış Rüzgar Türbini Palasında Performans Kayıp Analizi, VII. Ulusal Havacılık ve Uzay Konferansı (UHUK), Ondokuz Mayıs Üniversitesi, Samsun, Eylül, 2018.
2. Özcan YIRTICI and İsmail Hakkı TUNCER, RANS VE Pal Elemanları Yöntemi ile Yatay Eksenli Rüzgar Türbini Performans Analizi, VI. Ulusal Havacılık ve Uzay Konferansı (UHUK), Kocaeli Üniversitesi, Kocaeli, Eylül, 2016.
3. Özcan YIRTICI, Serkan ÖZGEN ve İsmail Hakkı TUNCER, NACA 0012 Kanat Profilinde Buz Birikimi Tahmini ve Performans Analizi, V. Ulusal Havacılık ve Uzay Konferansı (UHUK), Erciyes Üniversitesi, Kayseri, Eylül, 2014.
4. Özcan YIRTICI, Serkan ÖZGEN ve İsmail Hakkı TUNCER, Buzlanmış Kanat Profillerinde Performans Kayıp Analizi, HİTEK 2014, İstanbul, Haziran, 2014.

## **POSTER PRESENTATIONS**

1. Özcan YIRTICI, Serkan ÖZGEN, İsmail HAKKI TUNCER, Ice Accretion Prediction on Wind Turbine Blades Under Atmospheric Icing Conditions, 11. EAWE PhD Seminar on Wind Energy in Europe, 23-25 September 2015.